Finite Element Analysis of Adhesive Contact Interface in Continuous 3D Printing

by

Huifeng Du

Submitted to the Department of Mechanical Engineering
in partial fulfillment of the requirements for the degree of

Master of Science in Mechanical Engineering

at the

MASSACHUSETTS INSTITUTE OF TECHNOLOGY

May 2020

© Massachusetts Institute of Technology 2020. All rights reserved.

Author . . . .
Department of Mechanical Engineering
May 15, 2020

Certified by . . . .
Nicholas X. Fang
Professor
Thesis Supervisor

Accepted by . . . .
Nicolas Hadjiconstantinou
Chairman, Department Committee on Graduate Theses

Finite Element Analysis of Adhesive Contact Interface in Continuous 3D Printing

by

Huifeng Du

Submitted to the Department of Mechanical Engineering
on May 15, 2020, in partial fulfillment of the
requirements for the degree of
Master of Science in Mechanical Engineering

Abstract

Projection Micro-Stereolithography (PμSLA) is one of the most high-throughput additive manufacturing methods, yet preserving the high-resolution characteristic of light-based polymerization techniques. However, further improvement of fabrication speed and precision is usually hindered by the undesired adhesive forces at the curing interface, which is an inevitable consequence of *in situ* liquid-to-solid phase transition.

To overcome this limitation, a bio-inspired super low adhesive interface has been proposed based on the observation of a slippery water layer on the peristome surface of pitcher plant. This hydrophobic layer provides an effective shield to solid adhesion due to its low adhesive energy, and attracting force between fabricated part and UV curing interface is significantly reduced. The introduction of this new lubrication layer not only remarkably improves the fabrication speed, but also increases the refilling rate of liquid pre-polymer resin. This ultra-low adhesive interface shows promises for pushing the boundaries of continuous 3D printing into a realm of high-throughput additive manufacturing methods ready for industrial applications.

In this thesis, I sought to provide a more comprehensive understanding of the solid-solid interaction at the curing interface of 3D photo-polymerizing systems. The state-of-the-art review of current literature suggested that a surface-based cohesive contact theory from a continuum mechanics perspective was the most appropriate model to establish a connection between interfacial material properties and macroscopic measurement results from experiment. Based on that I analyzed the entire mechanical separation process using finite-element method, and provided a semi-quantitative explanation of the stability of such lubricant-infused nano-cavities against peeling forces. This research lays the ground for elucidating the physical mechanism behind the general adhesion-separation problem, and framework has been constructed in a more general form to allow for analyzing a wide range of interdisciplinary problems involving the dynamics of anisotropic moving contact lines and the propagation of surface instabilities induced by adhesive contact.

Thesis Supervisor: Nicholas X. Fang
Title: Professor

Acknowledgments

I would like to express my deep gratitude to my thesis and academic advisor, Prof. Nicholas Fang, for his long-time patience and thoroughness in guiding my research. He has always been supportive of my pursuit of scientific puzzle-solving driven by curiosity, and provided all essential resources for the completion of my work. I would've achieved nothing without his insightful perspectives and guidance.

I am also greatly indebted to my awesome collaborators Dr. Lei Wu, Dr. Zhichao Dong, Dr. Chuxin Li and Dr. Yanlin Song. Their experimental work formed the basis of this thesis, and they offered invaluable insights into the interpretation of the data. The dedication, scientific rigor and expertise they demonstrated have shaped the development of my research skills and led to the completion of this collaboration.

Last but not least, I would like to thank my family and friends who have always been standing by my side and cheering me up. Their unconditional support has significantly helped me walk through the hard times in my academic and daily lives. I would never have come this far without them.

Contents

1 Introduction and Background 17

1.1 Background 17

1.2 Microstereolithography 18

1.3 Challenges and constraints 21

1.4 Lubricant-infused Surfaces 24

1.5 Thesis Organization 25

2 Adhesive Contact Mechanics 27

2.1 Hertz Elastic Contact Model 28

2.2 Johnson-Kendall-Roberts (JKR) Model 29

2.3 Derjaguin-Muller-Toporov (DMT) Model 31

2.4 Bradley Model 32

2.5 Tabor Number 32

2.6 Maugis-Dugdale Theory and Cohesive Zone 34

2.6.1 Implementation in Abaqus FEA 38

3 Finite Element Analysis of Interfacial Damage during Separation Process in Continuous 3D Printing 43

3.1 Motivation for Adhesion Reduction Modeling and Sample Preparation in Continuous Stereolithography 44

3.2 Rational Selection of Contact Mechanics Models 48

3.3 Modeling of adhesion with Surface-based Cohesive Contact implementation in Abaqus 50

3.4 Analysis of Numerical Simulation Results 53
3.5 Summary and prospects 56

4 Conclusions and Future Work 61

List of Figures

1-1 Schematic of Projection Micro-Stereolithographic system. A digital model is sliced into layers. UV illumination implemented with digital mask carries the pattern from layered-image and is projected onto the resin interface. Solidified structure is elevated by a translation stage and separates the solid part from substrate. 20

1-2 Schematic of the cohesive zone at the resin-substrate interface. The undesirable adhesion force between different phases may damage the oxygen-inhibition surface, rupture the part and lower the printing resolution. 21

1-3 SEM images of surface of PDMS (a) before and (b) after continuous UV curing for 40 mm [44]. (c) Structural fracture in 3D biofabricated and polymerized hydrogel constructs due to oxygen inhibition [29]. . 22

1-4 Biological surfaces with micro- and nano-scale hierarchical architectures show tunable adhesive properties [10]. (a) Non-wetting and water-repellent legs of Water striders (*Gerris remigis*) [17]. (b) hierarchical structures in *Gekko gecko* enables robust and reversible adhesion [16]. (c) drag-reducing scales of sharks [36]. (d) Superhydrophobic surface of lotus (*N. nucifera*) leaf [11]. (e) sticky and also digestive glands of the carnivorous plants (*Drosera capensis*) [26]. 23

1-5 Liquid-infused surface coating: Applicable range, design parameters and tunability in biomedical applications [20]. 25

2-1 (a) Representative contact configuration of Hertz contact model, with a spherical indenter impounding on an elastic substrate. (b) Schematic of parabolic pressure distribution profile in the contact area. Maximum pressure is reached at the symmetry point of contact. 29

2-2 (a) Representative contact configuration of JKR contact model. A 'neck' area appears at the edge of contact when pulling up the object. (b) Schematic of parabolic pressure distribution profile in the contact area. Pressure remains positive at the center and negative (indicating tensile stress) near the edge. 30

2-3 Contact profile and stress distribution in DMT adhesive contact model. Hertzian contact stress is assumed within the contact region, while tensile stress derived from an interaction potential $V(z)$ exists outside this region. 31

2-4 Adhesion map of various adhesive contact models based on two dimensionless parameters. $\bar{P}$ is the total load divided by adhesion contribution part. δ_1 and h_0 are the elastic deformation and equilibrium distance, respectively [47]. δ_0 is the deformation caused by adhesion, and P_0 is a collective term of Hertz contact and Dugdale adhesive contact forces. 34

2-5 (a) Maugis-Dugdale contact model. Area of radius a denotes the contact section and attractive forces exist up to radius c (b)The stress distribution of Dugdale consists of Hertz pressure in a region of radius a and tensile traction when $a < r < c$, and the magnitude of constant traction is determined by matching the areas under curve with Lennard-Jones potential. 35

2-6 Different traction-separation laws based on cohesive zone concept. (a) Dugdale's constant stress. (b) Linear softening law. (c) Trapezoidal law and (d) Exponential law. 38

2-7 Schematic representation of the surface-based cohesive contact model implemented in SIMULIA Abaqus. ζ_c indicates the dissipated energy due to surface failure and numerically equals the area under the curve. Beyond the damage initiation point, red dashed line represents the linear damage evolution while blue dashed line corresponds to the exponential evolution law. 41

3-1 (a) Schematic of a typical bottom-up continuous 3D printing configuration. (b) Illustration of abnormal situations that could happen at the interface during separation. The unfavorable solid-solid adhesion may obstruct the refill flow of liquid resin into the gap and result in structural defects in the newly formed layer. Alternatively, when the adhesion at curing interface exceeds the bulk fracture strength of polymer or the bonding strength at the top, the part is mostly likely to rupture which invalidates the whole printing process. 45

3-2 (a) Side view of liquid resin refilling the 1 mm gap between printed part and a variety of testing surfaces: fluorinated PDMS, regular PDMS, fluorinated quartz, quartz and lubricant-infused PDMS. (b) Real-time phase front tracking of liquid contact line as it moves across the gap. Total length of slit is 1.4 cm. (c) Correlation between moving speed of support plate and projection light intensity in continuous 3D printing. (d) 3D representation of the variation of adhesive force based on different printing velocities and light intensities. 46

3-3 (a-b) Side view of the lubricant-infused PDMS and its enlarged local magnification. (c-d) Top view of the surface of lubricant-infused PDMS after treatment. (e) distribution of diameters of micro-holes. (f) Schematic of the Laplace pressure due to capillary effect that's holding back the liquid in the chamber. (g) A breakdown of the structural composition of the interfacial condition during 3D printing, and the illustration (h) showing the benefits of adhesion reduction along both normal and tangential directions. 47

3-4 (a) Map of various adhesive contact models based on net contact force and elasticity parameter. Material properties are plotted on the adhesion map based on estimation from experimental data. (b) Schematic of the contact geometry with parameters used in the definitions of two coordinates of the map. 50

3-5 (a) Configuration of the simulation. Photopolymer (cylindrical object) is in contact with the substrate (cuboid). (b)The constitutive relation in surface-based cohesive contact model (c) Schematic of the pulling up and deforming process during separation process in 3D printing. (d) Molecular picture of the cohesive interaction at the interface between photopolymer and substrate. 52

3-6 Von Mises stress distribution for different substrate modifications: (a) Regular PDMS (b) fluorinated PDMS (F-PDMS) and (c) ultra-low adhesive energy interface (S-PDMS). Deformation field is magnified 5 times. 54

3-7 (a)Schematic of the experimental setup for force-displacement curve measurement. (b) Plotted experimental data of force and displacement in the peel-off test. Violet, magenta, black, red, orange and blue lines are force-displacement curves of Quartz, F-quartz, PDMS, F-PDMS, silicone oil swelled PDMS and the ultra-low adhesive S-PDMS interfaces, respectively. The data of quartz-based surfaces use the axis on the left and the data of the PDMS-based surfaces use the axis on the right and simulated results in (c). 56

3-8 (a-h)Comparison of different interfaces during UV curing process. I shows different contact modes of impinging droplet on surfaces. II and III are optical images of resin morphology after plate has been lifted for a corresponding value of distance. [44] (i-j) Image sequences showing different transient liquid profiles of capillary thinning and breakup process for (i) Newtonian filament and (j) Boger fluid. [3] 58

3-9 Long-term force-displacement curves for different interfaces during a complete continuous 3D printing process. Inset is the enlarged part of the force-displacement curve between 20 - 40 mm region for PDMS, F-PDMS and Silicone oil-PDMS surface. Violet, magenta, black, red and orange lines are force-displacement curves of Quartz, F-quartz, PDMS, F-PDMS and the silicone oil swelled PDMS interfaces, respectively. . 59

4-1 (a) Schematic of wrinkle of surface during adhesive contact. (b) Lateral force variable during rubber sliding and representative images of contact area. Scale bar 250 µm [35]. (c) Distortion of grid in a transparent rubbery material deformed by a rigid slider. [37]. (d) Wave front of Schallamach waves generated by a cylinder lens sliding on elastomer. Top row shows a solitary wave propagation and bottom panel is three-dimensional intensity plot of contact area morphology.A is undisturbed initial contact, and B is the wave front and C contains air cavities. E shows damaged surface after contact separation/wave passage and re-enter of adhesion. [41] 63

List of Tables

1.1 Listing of major fabrication methods for bio-mimetic low-adhesion surfaces 24

2.1 Conversion table for variants of Tabor number definitions 33

3.1 Listing of all the criteria for determination of boundaries between different adhesive models. Additional equation is required to solve for the plot axis parameter. Separation criteria from [24]. 49

3.2 Listing of all the interfacial parameters for various surfaces simulated in this work. S-PDMS is the lubricant-infused PDMS and all the rest in the control groups are plain quartz surface (Quartz), fluorinated quartz surface (F-Quartz), untreated PDMS surface, and the fluorinated PDMS (F-PDMS) surface. 52

Chapter 1

Introduction and Background

1.1 Background

Slippery surfaces with low adhesive energy widely exist in nature. The surface of lotus leaves consisting of air-infused micro-solid structures effectively reduce the surface frictional resistance and provide lubrication to impinging liquid droplet. This type of biological surfaces are usually known as superhydrophobic structures with large liquid contact angle and water-repelling capability. Similarly, certain rose petals have superhydropobic surfaces with either high or low adhesion depending on the pitch value and density of their hierarchical structures [9]. Sharks are able to swim fast and efficiently in water due to the riblet structures on their skins. The tooth-like denticles and scales reduce the skin friction drag in the turbulent-flow regime, and the presence of mucus on the skin as a hydrophobic layer is also beneficial to the further reduction of drag force during locomotion [15].

The ability to generate a mucous layer for lubrication and protection is not unique to animals. *Nepenthes*, also known as pitcher plants, has a slippery water layer on the peristome surface which causes insects to slide on into the chamber filled with digestive liquid. The slippery surface has aroused interests in material scientists and engineers who try to investigate its slippery behavior. In addition to the less-sticking nature of the surface, the underlying solid substrate is free from direct contact with the other substances on top, and researchers find that we could replicate pitcher plant's shielding behavior in many application scenarios where lower adhesion and more insulation of substrate material are favorable. For example, in additive manufacturing there's usually a strong adhesive force between formed solid structure and the interface where solidification happens, and reducing adhesion is essential to the improvement of resolution and yield of 3D printing technologies.

The fundamental aim of this research was to review the contact mechanics models which most suitably depicts the mechanical behavior of impinging solids coming into contact with the slippery layer, and to develop a methodology for modeling the separation process, specifically in 3D printing with the low adhesive energy interface between cured resin and substrate. There have been many research efforts to mimic the non-sticking behavior of natural systems [43] [42] [13] [38], yet the specific physical mechanism of remains to be elucidated. Besides, the vast range of material types encountered in additive manufacturing requires a universal solution to generate a curing interface that is suitable for arbitrary materials in interaction. Thus this thesis was organized into three parts to achieve the research aim:

1. Introduction of 3D printing techniques and the experimental preparation of slippery surface
2. Various contact-mechanics modelings of adhesion force
3. Develop a framework for analyzing the general contact-separation problem and providing insights for implementation into 3D printing

1.2 Microstereolithography

Microstereolithography is a novel form of additive manufacturing techniques. This nomenclature indicates it is based on conventional lithographic principles with 3D fabrication capability. Either by scanning concentrated light spot in the bathe or projecting modulated light on the surface of photosensitive liquid resin, the energies of the photons are selectively absorbed in specific region, which induces the chemical reaction and initiates the bonding of short molecules into cross-linked polymer chains. Consequently, exposed areas are solidified into the patterns carried by light.

A typical microstereolithography fabrication process usually starts from disintegrating a computer-aided design (CAD) model into either raster-based or vector-based images. Due to this 3D to 2D transition, microstreolithography is often characterized as a Layered Manufacturing Technique [Gibson, P41, Ref 8,9], in the sense that it reconstructs a 3D structures layer by layer. After obtaining the discretized data of the 3D model, each single layer is fabricated by lateral movement of the light beam controlled with scanning mirrors. Alternatively, instead of moving the illumination voxel back and forth, the whole layer can be polymerized with a single exposure of the raster image. Therefore a mask, physical or digital, needs to be present to modulate the illumination light so it carries the desired pattern of this layer. Once a layer is built, a piezoelectric actuator from which the building platform is mounted will move on to the next layer the above process is repeated until the whole part is finished.

Depending on the ways light is projected and whether a photo-mask is adopted, a fabrication method can be either based on vector tracing of light beam, where an individual layer is solidified by scanning of illumination voxel across the plane, or projection of the pattern through a (digital) mask which polymerizes the whole layer with a single exposure. These two main classes are characterized by two representative technologies, Direct Laser Writing (DLW) and Projection Microstereolithography (PuSL).

For photo-polymerization, it is novel solid freeform fabrication technique assisted by digital micro-mirror dynamic mask, and sometimes the term stereolithography is interchangeably used. Basically, the polymerization of the pre-polymer solution is induced by concentrated light spot [Sun et al. 2005], and 3D structures are formed by scanning of the illuminated point inside the photo curable resin along pre-designed path. With precise optical control, micron-scale resolution has been successfully achieved, and sub-micron structure was reported by using two-photon absorption as the polymerization mechanism [citation needed]. In practice, stereolithography outweighs any other SFF techniques for organ printing in that it has the best in-

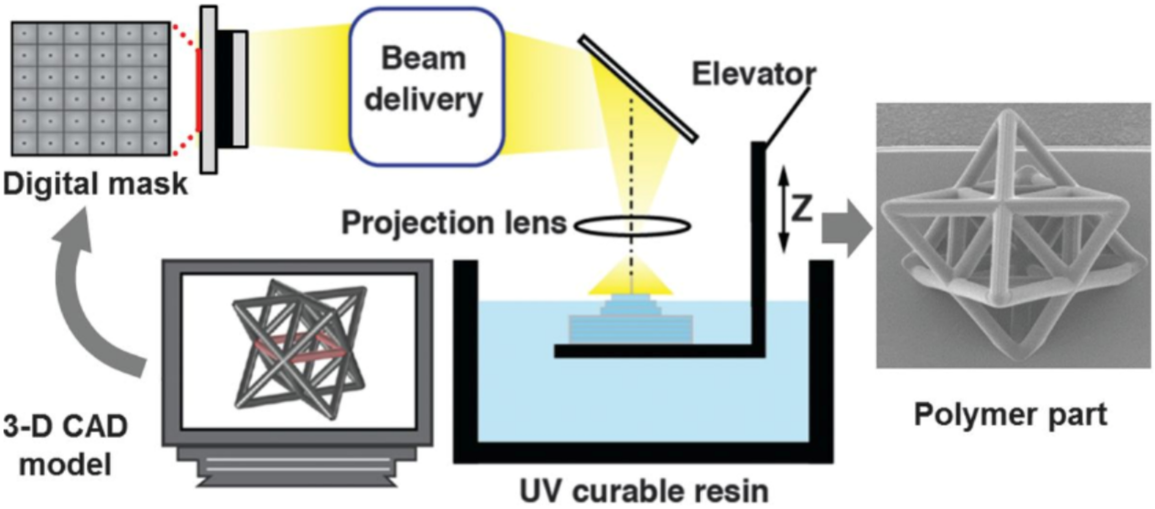

Figure 1-1: Schematic of Projection Micro-Stereolithographic system. A digital model is sliced into layers. UV illumination implemented with digital mask carries the pattern from layered-image and is projected onto the resin interface. Solidified structure is elevated by a translation stage and separates the solid part from substrate.

plane resolution [citation needed], but the serial fabrication nature and consequent low speed limit its potential applications.

To overcome these drawbacks of this point-to-point technique, projection micro-stereolithography (PuSL) is developed. Like the other 3D printing techniques, masks patterns of the complex 3D structures are determined by slicing the CAD design model with a series of closely spaced horizontal planes and taking them in electronic format. Light is shaped according to the mask patters and is transferred to form an image on photo-curable resin surface. In each layer, the illuminated area is solidified simultaneously under one exposure. Subsequent layers are fabricated using the same step by gradually immersing the solidified part into light curable resin. As the crosslinking in the pre-polymer solution is induced by exposure to UV light, the materials compatible with PuSL are limited to some photo-polymers, including PRG, PLA, PCL and some other commonly used polymers which are bio-compatible as well as bio-degradable [Xia et al. 2005, also citing something up-to-date here]. However, some researchers also demonstrated the possibility of manufacturing metal/ceramic structures with PuSL (citing Fang 2014 Science, et al.)

1.3 Challenges and constraints

Depending on the UV projection direction, Digital Light Processing (DLP) 3D printing can be categorized into top-down approach, where the curing process occurs at the top liquid resin-air interface, and the bottom-up approach with polymerization happening at the liquid-solid interface at the bottom of resin chamber. During a top-down 3D printing process, the part holder is moving downwards with the cured model remaining immersed in the resin pool. Therefore, the original resin depth should be larger than the height of the designed structure. A typical working cycle in 3D printing usually takes hours long, and the vast volume of liquid resin was rendered unrecyclable due to excessive exposure to unwanted background light. In addition, curing takes place at the liquid-air interface, which is essentially sensitive to ambient vibration. Under these considerations, the bottom-up configuration is frequently implemented, as illustrated by Figure 1-2.

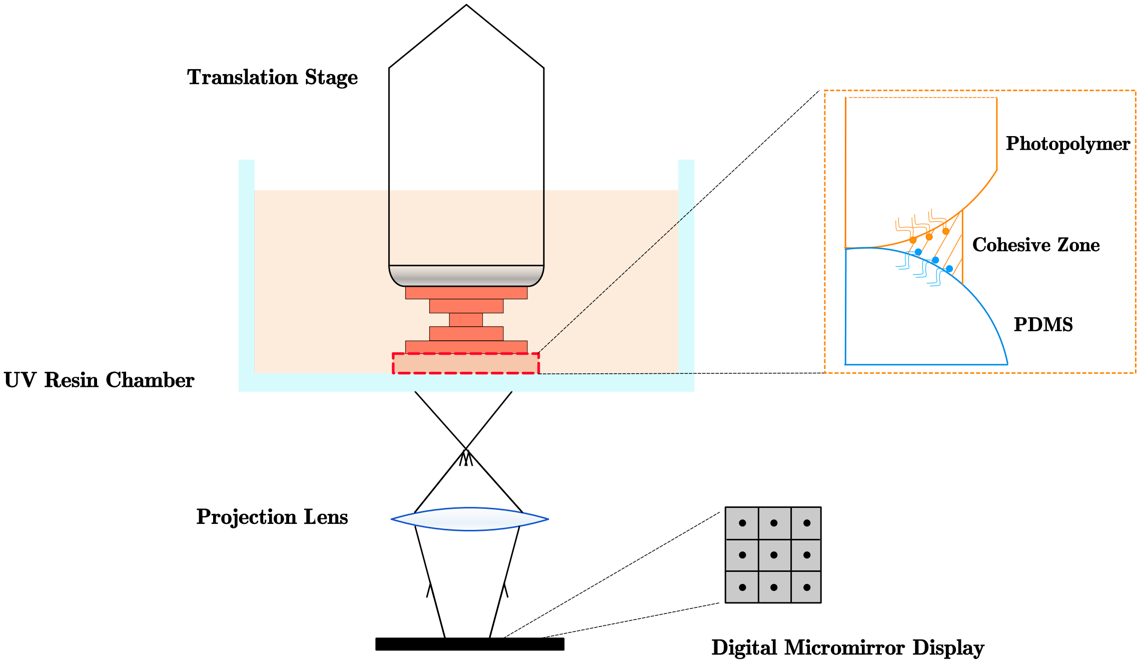

Figure 1-2: Schematic of the cohesive zone at the resin-substrate interface. The undesirable adhesion force between different phases may damage the oxygen-inhibition surface, rupture the part and lower the printing resolution.

Even though they are effective in constructing high resolution structures in X-Y plane, such bottom-up DLP based additive manufacturing methods still have to overcome several critical challenges, such as limited process speed due to repeated pulling up and down process, low Zaxis resolution, and anisotropic mechanical property, which are essentially originated from the adhesion at the curing interface.

A concurrent variation of the PuSL system features a bottom-up configuration, and silicone rubbers like polydimethylsiloxane (PDMS) are commonly used as substrate for their oxygen-inhibition capability. This surface, however, is not immune to contamination and damage induced by sudden rupture of the cohesive layer between cured solid and PDMS. In addition, PDMS naturally absorbs small molecules and dyes in the photoresin, which results in the degradation of printing resolution over time.

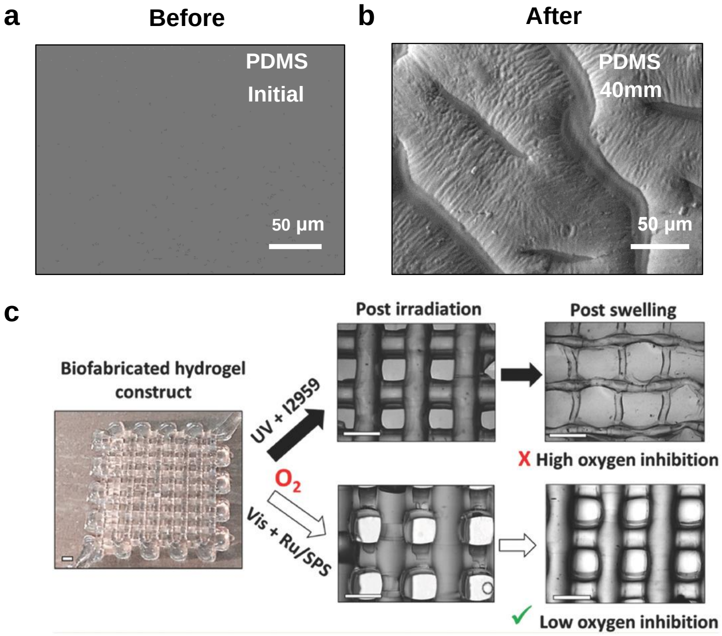
a
Before
PDMS
Initial
50 μm
b
After
PDMS
40mm
50 μm
c
Biofabricated hydrogel construct
UV + I2959
O_2
Vis + Ru/SPS
Post irradiation
Post swelling
X High oxygen inhibition
✓ Low oxygen inhibition

Figure 1-3: SEM images of surface of PDMS (a) before and (b) after continuous UV curing for 40 mm [44]. (c) Structural fracture in 3D biofabricated and polymerized hydrogel constructs due to oxygen inhibition [29].

Several studies are dedicated to the understanding of low-adhesion interfacial phenomena in nature and outline the fabrication processes for the preparation of non-sticking surfaces. Figure 1-4 summarizes examples of naturally occurring surfaces with water-repellent and self-cleaning capabilities. There are many engineering ef-

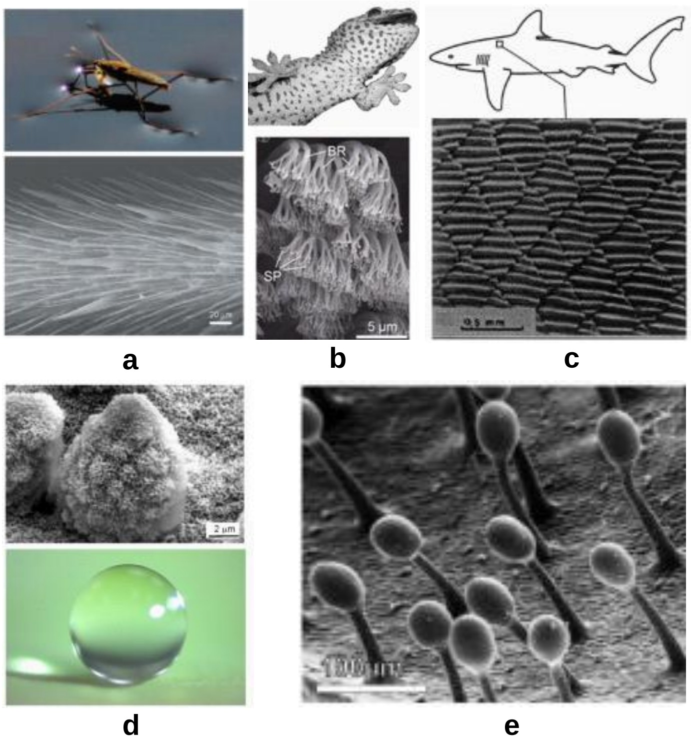

Figure 1-4: Biological surfaces with micro- and nano-scale hierarchical architectures show tunable adhesive properties [10]. (a) Non-wetting and water-repellent legs of Water striders (*Gerris remigis*) [17]. (b) hierarchical structures in *Gekko gecko* enables robust and reversible adhesion [16]. (c) drag-reducing scales of sharks [36]. (d) Superhydrophobic surface of lotus (*N. nucifera*) leaf [11]. (e) sticky and also digestive glands of the carnivorous plants (*Drosera capensis*) [26].

forts to produce such superhydrophobic interfaces inspired by and mimicking the behavior of their biological counterparts. Micro- and nano-fabrication techniques including lithography, etching, deposition, deformation and transfer, enables the direct fabrication of single- and multiple-scales on a surface, and we summarize the essential features of these technologies in the following table (adapted from [10]):

Although these techniques are effective in generating ultra low-adhesion interfaces resembling the normal adhesive energy of actual gecko foot, they inevitably require sophisticated experimental facilities and exhibit poor control over the process. Additionally, the engineered superhydrophobic surfaces suffer severe degradation due to

Methods	**Adhesive Energies** ($\mathrm{N\,cm^{-2}}$)	**Limitations**
Lithography	1-10 [18, 14, 28]	Expensive and slow process
Etching	0.7 [27]	Chemical contamination, less control
Deposition	10 [34], 12-29 [33]	Possible temperature rise, less control
Gecko foot	10 [5, 6]	-

Table 1.1: Listing of major fabrication methods for bio-mimetic low-adhesion surfaces

friction and wear, so that the durability and maintenance of such surfaces in practical applications become a unavoidable challenge [31].

1.4 Lubricant-infused Surfaces

To address the issues associated with artificially-introduced hierarchical structures,, lubricant-infused materials have recently emerged as an effective alternative. As a type of liquid-repellent coating, it's usually working by the confinement of an immiscible and non-reactive liquid lubricant overlayer onto a solid substrate to shield it from being in contact with the contaminating medium, and the retention of lubricant liquid into substrates under preparation can be achieved either via van der Waals forces or joint infusion of another polymer to form three-dimensional gel network [2].

Due to the general applicability on a wide range of interfaces and stability against frictional wear-off, liquid-infused coating methods are gaining attention for broad applications in different fields. These include mitigation of biofouling [2], anti-corrosion [45], self-healing [21] and adhesion-resistant biomedical devices [46]. Howell *et al.* summarized the adaptability and design parameter-space of such interface-modifying strategy: Since these slippery surfaces can protect underlying solid substrate from absorbing small molecules and being attached to by impinging liquids or solids, it could provide a feasible solution to the sticking issues commonly experienced during photopolymerization-based 3D printing as stated in the earlier part of this chapter. Therefore, this thesis is dedicated to the understanding of the adhesive contact mechanics in the context of continuous 3D printing. As a part of an earlier published work, we specifically explore the photo-curing induced adhesion at the curing boundary, and demonstrate that a ultra-low adhesive energy interface facilitates de-

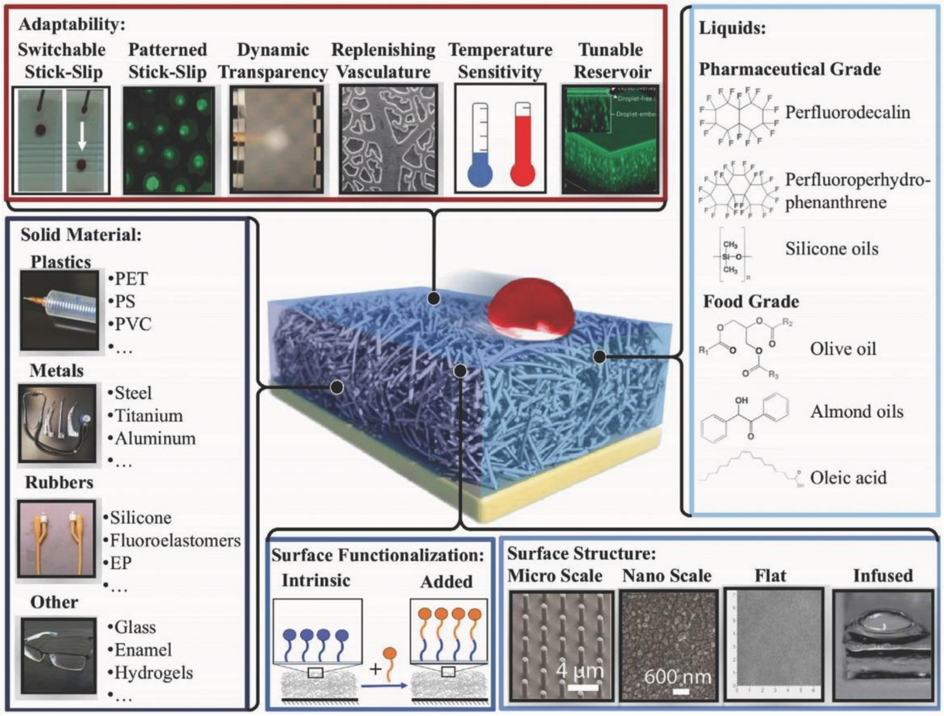
Adaptability:
Switchable Stick-Slip
Patterned Stick-Slip
Dynamic Transparency
Replenishing Vasculature
Temperature Sensitivity
Tunable Reservoir
Liquids:
Pharmaceutical Grade
Perfluorodecalin
Perfluoroperhydro-phenanthrene
Silicone oils
Food Grade
Olive oil
Almond oils
Oleic acid
Solid Material:
Plastics
•PET
•PS
•PVC
•...
Metals
•Steel
•Titanium
•Aluminum
•...
Rubbers
•Silicone
•Fluoroelastomers
•EP
•...
Other
•Glass
•Enamel
•Hydrogels
•...
Surface Functionalization:
Intrinsic
Added
Surface Structure:
Micro Scale
Nano Scale
Flat
Infused
4 μm
600 nm

Figure 1-5: Liquid-infused surface coating: Applicable range, design parameters and tunability in biomedical applications [20].

tachment of solidified polymer parts, thus accelerates the liquid resin refill and the whole fabrication process in general.

1.5 Thesis Organization

This thesis will be presented in the following organizational structure. Chapter 2 discusses the general contact mechanics models to characterize the solid-solid contact with adhesion, along with theoretical studies of the mechanisms of lubricant-infused surfaces.Chapter 3 develops a finite-element framework for the analysis of the attach-separation behavior at the polymerization interface, and describes the details of implementing such numerical model. Chapter 4 incorporates the finite-element model into analysis of the adhesion reduction at interface during continuous 3D printing and interprets the experimental data. Chapter 5 provides a summary of the work in this thesis, with comments on the insights of this study and future directions.

Chapter 2

Adhesive Contact Mechanics

The adhesion contact mechanics deals with the deformation of bodies coming into contact with each other when attractive coupling is present. Non-adhesive contact theories like Hertz model show discrepancies with experimental measured values especially at low loading regime. Observations are that the real contact area tends to be larger than predicted by those theories, and that they do not go back to zeros even when external loading is removed. This phenomenon indicates there are additional unaccounted for attractive forces (for example, van der Waals forces between atoms or molecules) at interface, which prompts for amendments to existing theories to address the contradictions.

Since many of the linear elastic models of adhesion derive and evolve from Hertz model, we first start this chapter with a brief review of Hertz contact theory, and then proceed to Johnson-Kendall-Roberts (JKR) model of elastic contact, DMT (Derjaguin–Muller–Toporov) model and Bradley model. These theories don't agree at all times, and Tabor [40] proposed a dimensionless number to account for the discrepancy and govern the transition process. Maugis-Dugdale theory provides analytical results in the intermediate regions where Tabor number has moderate values.

2.1 Hertz Elastic Contact Model

Hertz (1896) made the following assumptions regarding two bodies in contact. For the calculation of local deformations, each body can be treated as an elastic half space. The loaded contact area is an elliptical region with no adhesive or frictional forces. In the simple case of contact solids revolution (two spheres, for example), the distribution of pressure reads as:

$$p = p_0 \left\{ 1 - \frac{r^2}{a^2} \right\}^{1/2} \tag{2.1}$$

with the contact radius a, mutual approaching distance (or indentation depth in some contexts) δ and maximum pressure p_0 written as:

$$a = \left(\frac{3FR}{4E^*} \right)^{1/3} \tag{2.2}$$

$$\delta = \frac{a^2}{R} = \left(\frac{9F^2}{16RE^{*2}} \right)^{1/3} \tag{2.3}$$

$$p_0 = \frac{3F}{2\pi a^2} = \left(\frac{6FE^{*2}}{\pi^3 R^2} \right)^{1/3} \tag{2.4}$$

In the above expressions, $1/R = 1/R_1 + 1/R_2$ is the inverse effective radius, $1/E^* = (1 - \nu_1^2)/E_1 + (1 - \nu_2^2)/E_2$ applies when one of the bodies is not rigid, and F is the total indenting force, as shown in the Figure 2-1:

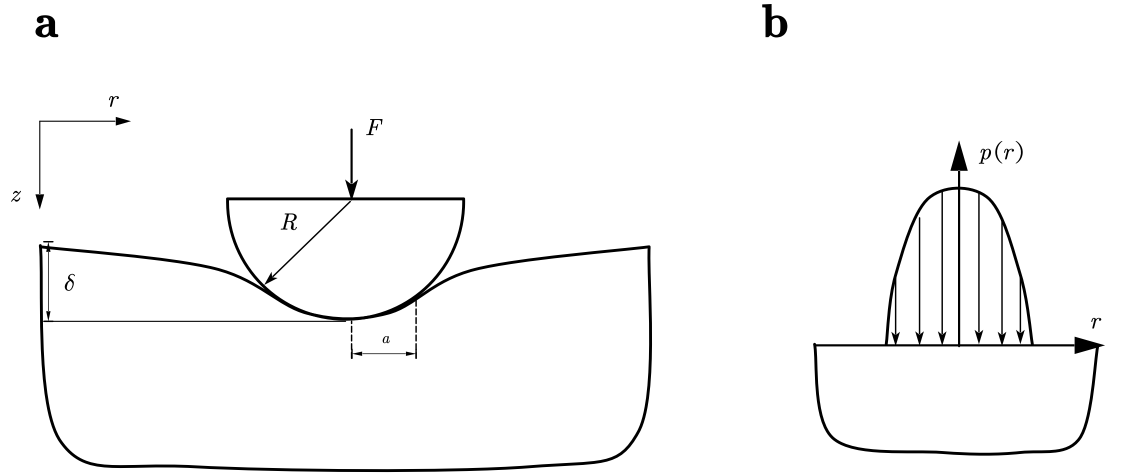

Figure 2-1: (a) Representative contact configuration of Hertz contact model, with a spherical indenter impounding on an elastic substrate. (b) Schematic of parabolic pressure distribution profile in the contact area. Maximum pressure is reached at the symmetry point of contact.

Regarding more general cases, Hertz assumed the contact area takes an elliptical shape as well as the pressure distribution profile. The detailed derivations are well documented [22] thus will not be repeated here.

2.2 Johnson-Kendall-Roberts (JKR) Model

Several contradictions of Hertzian contact have been reported ever since the publishing of the theory. In an adhesive hemisphere contact experiment, Roberts (1968a) observed the formation of a neck at the edge of contact (illustrated in Figure 2-2), and the area were considerably larger than Hertz's prediction when load was approaching zero. Strong adhesion effects became particularly obvious at low loads. In an approach analogous to the analysis of surface wetting, Johnson, Kendall, and Roberts [23] treated the adhesion as a balance of stored elastic deformation energy and surface energy. A direct modification to Hertz model would be the addition of a negative flat punch indentation term to the pressure distribution. For a circular contact [25] (which allows for straightforward comparison with previous section),

$$p(r) = p_h \left(1 - \frac{r^2}{a^2}\right)^{\frac{1}{2}} - p_a \left(1 - \frac{r^2}{a^2}\right)^{-\frac{1}{2}} \tag{2.5}$$

with $p_h = \frac{2aE^*}{\pi R}$ being the original Hertzian contact and $p_a = \left(\frac{2\Delta\gamma E^*}{\pi a}\right)^{\frac{1}{2}}$ is the new surface energy ($\Delta\gamma$) contribution due to adhesion. Negative sign indicates the tension is pulling the contact surfaces back together. The area of contact then can be expressed as:

$$a^3 = \frac{3R}{4E^*}(F + 3\Delta\gamma\pi R + \sqrt{6\Delta\gamma\pi RF + (3\Delta\gamma\pi R)^2}) \tag{2.6}$$

which also implies that in order to obtain a real solution, the applied load has to satisfy

$$F \geq -\frac{3}{2}\Delta\gamma\pi R \tag{2.7}$$

This is also the critical tensile load for separation to occur.

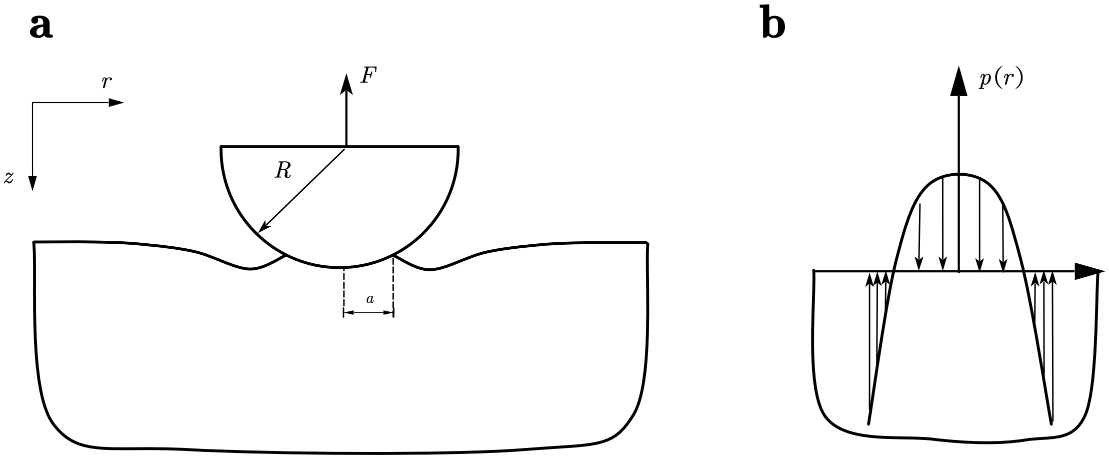

Figure 2-2: (a) Representative contact configuration of JKR contact model. A 'neck' area appears at the edge of contact when pulling up the object. (b) Schematic of parabolic pressure distribution profile in the contact area. Pressure remains positive at the center and negative (indicating tensile stress) near the edge.

2.3 Derjaguin-Muller-Toporov (DMT) Model

In 1975 and 1983, Derjaguin, Muller and Toporov collaboratively proposed an extension of an early theory of Derjaguin. They hypothesized that Hertzian stress distribution and contact profile applies within the contact region, while additional adhesive interactive results in attractive forces outside the region (Figure 2-3)

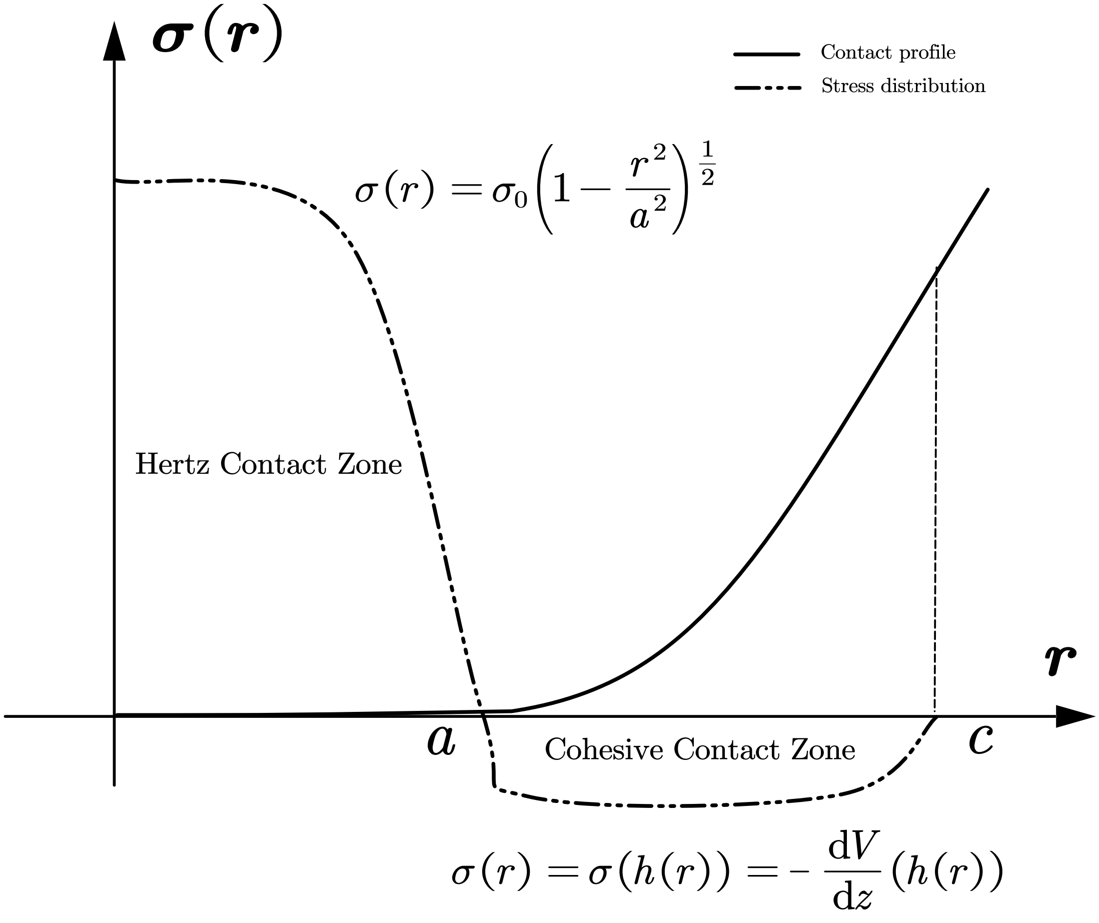

$\boldsymbol{\sigma}(\boldsymbol{r})$
Contact profile
Stress distribution
$\sigma(r) = \sigma_0\left(1 - \frac{r^2}{a^2}\right)^{\frac{1}{2}}$
Hertz Contact Zone
$\boldsymbol{r}$
a
Cohesive Contact Zone
c
$\sigma(r) = \sigma(h(r)) = -\frac{\mathrm{d}V}{\mathrm{d}z}(h(r))$

Figure 2-3: Contact profile and stress distribution in DMT adhesive contact model. Hertzian contact stress is assumed within the contact region, while tensile stress derived from an interaction potential $V(z)$ exists outside this region.

A major difference from JKR model is that in DMT model, adhesion only exists outside the contact area. Contact radius, indentation depth and pull-off force can be written as:

$$a^3 = \frac{3R}{4E^*}(F + 2\Delta\gamma\pi R) \tag{2.8}$$

$$\delta = \frac{a^2}{R} = \left(\frac{3}{4E^*}\left(\frac{F}{\sqrt{R}} + 2\Delta\gamma\pi\sqrt{R}\right)\right)^{2/3} \tag{2.9}$$

$$F_{\text{pull-off}} = -2\Delta\gamma\pi R \tag{2.10}$$

2.4 Bradley Model

In an early pioneering work, Bradley [12] calculated the adhesive force between two spheres The similarity between Bradley's and Derjaguin's approaches is that they simultaneously considered the interaction potential $V(z)$ between two surfaces in contact [8]. For example, consider Lennard-Jones form of stress:

$$\sigma(h) = -\frac{8\Delta\gamma}{3\varepsilon}\left[\left(\frac{\varepsilon}{h}\right)^3 - \left(\frac{\varepsilon}{h}\right)^9\right] \tag{2.11}$$

The force between two rigid spheres separated by a distance of h_0,

$$F\left(h_0\right) = 2\pi R\int_{h_0}^{\infty}\sigma(h)\mathrm{d}h = -2\pi R\Delta\gamma\left[\frac{4}{3}\left(\frac{\varepsilon}{h_0}\right)^2 - \frac{1}{3}\left(\frac{\varepsilon}{h_0}\right)^8\right] \tag{2.12}$$

When two spheres are in contact, Bradley treated h_0 to be the interatomic separation ε and arrived at the force:

$$F_c = F\left(h_0 = \varepsilon\right) = -2\pi R\Delta\gamma \tag{2.13}$$

Note it has the same form as the pull-off force in the DMT model.

2.5 Tabor Number

The pull-off forces derived from JKR model ($\frac{3}{2}\pi R\Delta\gamma$) and DMT or Bradley models ($2\pi R\Delta\gamma$) apparently contradicted each other. This discrepancy was later resolved by Tabor when he proposed a governing dimensionless number defined by [40]

$$\mu = \left(\frac{R(\Delta\gamma)^2}{E^{*2}\varepsilon^3}\right)^{1/3} \tag{2.14}$$

Physically, the Tabor number can be considered as the ratio of neck height in JKR contact to the interatomic separation ε,

$$\mu = \frac{h^*}{\varepsilon} = \left(\frac{R(\Delta\gamma)^2}{E^{*2}}\right)^{1/3} / \varepsilon = \left(\frac{R(\Delta\gamma)^2}{E^{*2}\varepsilon^3}\right)^{1/3} \tag{2.15}$$

Several variants of Tabor number have been reported, and Greenwood [19] summarized a conversion table from published works:

Symbols and equation	**Conversion**	**References**
$\mu = \left(\frac{R(\Delta\gamma)^2}{E^{*2}\varepsilon^3}\right)^{\frac{1}{3}}$	-	[40]
$\mu_{\mathrm{T}} = \left(\frac{6\pi^2 R(\Delta\gamma)^2}{E^{*2}\varepsilon^3}\right)^{\frac{1}{3}}$, neck height to interatomic separation	$\mu_{\mathrm{T}} = 3.898\mu$	[32]
$\mu_{\mathrm{D}} = \frac{32}{3\pi}\left(\frac{2R(\Delta\gamma)^2}{\pi E^{*2}\varepsilon^3}\right)^{\frac{1}{3}}$, atomic tearing-off force to adhesion force	$\mu_{\mathrm{D}} = 2.9208\mu$	[32]
$\lambda = \left(\frac{9}{2\pi}\frac{R\sigma_0^3}{E^{*2}\Delta\gamma}\right)^{\frac{1}{3}}, \quad \sigma_0 = \frac{16}{9\sqrt{3}}\frac{\Delta\gamma}{\varepsilon}$, similar to μ_{D}	$\lambda = 1.157\mu$	[30]
$\lambda' = \frac{\Delta\gamma}{2E^*}\left(\frac{R}{\varepsilon^3}\right)^{\frac{1}{2}}$, variant of μ_{T}	$\lambda' = 0.5\mu^{3/2}$	[4]

Table 2.1: Conversion table for variants of Tabor number definitions

Though the detailed expressions differ, Tabor number generally measures the relative importance of adhesive interaction to the elastic deformation, and guides the transition between different adhesion models. When the contacts bodies are stiff and elastic deformation is negligible, μ is small and the Bradley rigid contact theory applies; For small adhesion, the Derjaguin-Muller-Toporov (DMT) model provides a good approximation while for highly adhesive between soft bodies Johnson-Kendall-Roberts (JKR) theory becomes the approximate model of description. The relationships have been illustratively represented by the following phase map [24]:

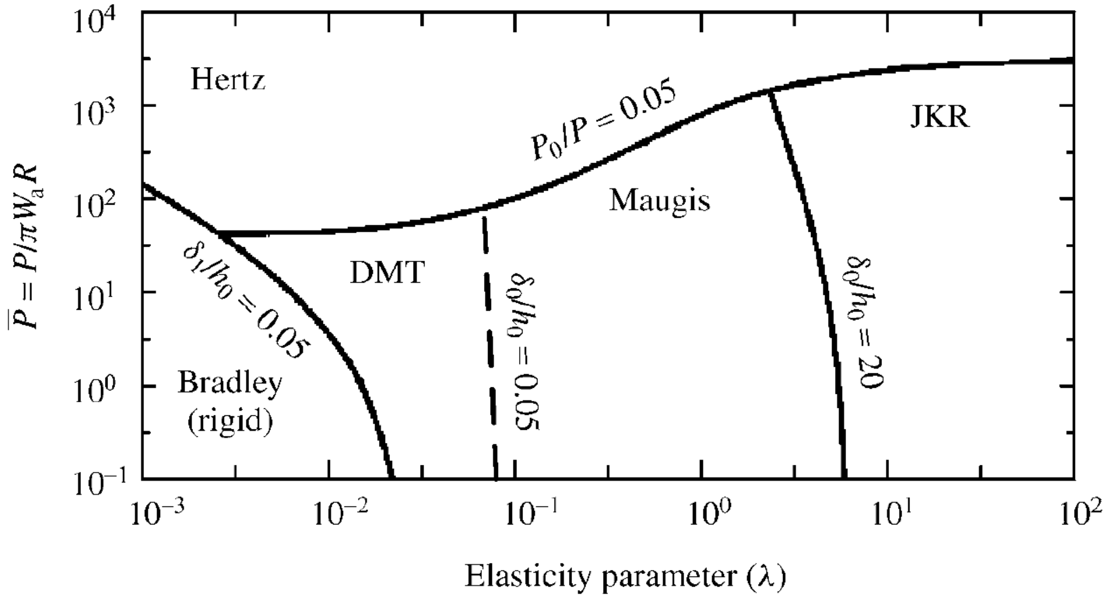

Figure 2-4: Adhesion map of various adhesive contact models based on two dimensionless parameters. $\bar{P}$ is the total load divided by adhesion contribution part. δ_1 and h_0 are the elastic deformation and equilibrium distance, respectively [47]. δ_0 is the deformation caused by adhesion, and P_0 is a collective term of Hertz contact and Dugdale adhesive contact forces.

This adhesion phase map allows the rational selection of contact models based on characteristic material properties and loading conditions.

2.6 Maugis-Dugdale Theory and Cohesive Zone

In Figure 2-4, the transition between DMT and JKR models are governed by Maugis contact, which was proposed by Maugis [30] as an extension of Dugdale's early study. The attractive stress outside contact area was assumed to be constant. For circular contact between two spheres of reduced radius $R = 1/(1/R_1 + 1/R_2)$, [24]

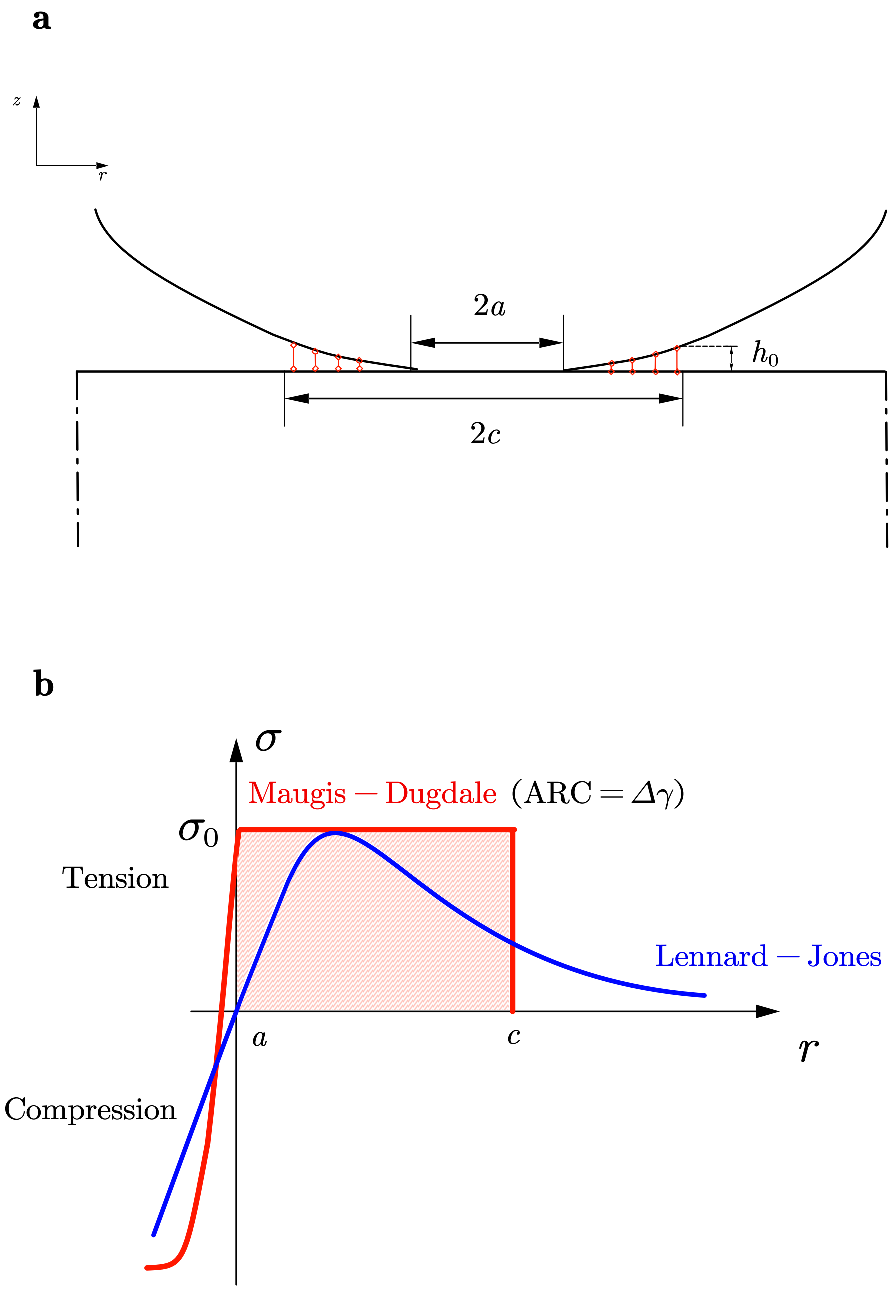
a
z
r
2a
h_0
2c
b
σ
Maugis − Dugdale (ARC = $\Delta\gamma$)
σ_0
Tension
Lennard − Jones
a
c
r
Compression

Figure 2-5: (a) Maugis-Dugdale contact model. Area of radius a denotes the contact section and attractive forces exist up to radius c (b)The stress distribution of Dugdale consists of Hertz pressure in a region of radius a and tensile traction when $a < r < c$, and the magnitude of constant traction is determined by matching the areas under curve with Lennard-Jones potential.

The model assumes the stress distribution consists of two contributions: Hertz contact pressure for $0 \leq r < a$ and Dugdale form of adhesive stress:

1. Hertz contact pressure:

$$p_H(r) = \frac{3P_H}{2\pi a^2}\left\{1 - \frac{r^2}{a^2}\right\}^{1/2}, P_H = 4E^* a^3/3R \tag{2.16}$$

with elastic compression due to indentation, normal displacement at $r = c$ and gap between two interfaces at same location being:

$$\delta_H = u_{z1}(0) = a^2/R \tag{2.17}$$

$$u_z^H(c) = (1/\pi R)\left\{\left(2a^2 - c^2\right)\sin^{-1}(a/c) + a\sqrt{c^2 - a^2}\right\} \tag{2.18}$$

$$h_H(c) = c^2/2R - \delta_1 + u_{z1}(c) \tag{2.19}$$

2. Contribution from adhesive Dugdale stress,

$$p_{\mathrm{D}}(r) = \begin{cases} -\frac{\sigma_0}{\pi} \quad \cos^{-1}\left\{\frac{2a^2-c^2-r^2}{c^2-r^2}\right\}, & r \leq a \\ -\sigma_0, \quad a \leq r \leq c \end{cases} \tag{2.20}$$

Similarly, the indentation depth and gap between surfaces are

$$\delta_{\mathrm{D}} = -\left(2\sigma_0/E^*\right)\sqrt{c^2 - a^2} \tag{2.21}$$

$$h_{\mathrm{D}}(c) = \left(4\sigma_0/\pi E^*\right)\left\{\sqrt{c^2 - a^2}\cos^{-1}(a/c) + a - c\right\} \tag{2.22}$$

The combined traction is thus the sum of Hertzian and Dugdale's contribution terms: $p(r) = p_H(r) + p_{\mathrm{D}}(r)$, and the same rule applies for the total force. We can also express the maximum distance of separation h_0 as

$$h(c) = h_H(c) + h_{\mathrm{D}}(c) = h_0 = \Delta\gamma/\sigma_0 \tag{2.23}$$

Maugis [30] also proposed a set of dimensionless parameters to non-dimensionalize the above equations, from which we see that as elasticity parameter λ becomes large, Maugis-Dugdale model reduces to JKR model while when λ is small Bradley's contact is reproduced. Thus the Maugis-Dugdale theory of contact constitutes the bridge between two prevalent adhesion models and guides the transition between them depending on the competition between elastic deformation due to adhesion and effective range of interaction forces along the tangential of interface. Later studies extend the theories of Dugdale (1960) and Barenblatt (1962) [7] to characterize the initiation and completion of separation process beyond the crack tip, now collectively known as cohesive zone model. It hypothetically treats the cohesive zone as two geometrical surfaces held together by adhesive forces ahead of the pre-existent crack tip. The separation law dictates the relationship between relative displacement and surface traction at the interface. As the two surfaces are being teared apart by external loads, the separation distance at the end of cohesive zone reaches a critical value and hence the crack grows and propagates inside the bulk material. Compared with conventional Linear Elastic Fracture Mechanics (LEFM) theories, cohesive zone model bypasses the challenges involved in the physical interpretation of stress singularity at the perfectly sharp crack tip [39]. The energy dissipation mechanism is readily incorporated in this model, as the interfacial displacement-traction constitutive relations enable direct integration of the work required to create new surfaces.

Apart from Dugdale's constant adhesive stress model, there are several other commonly encountered separation laws that are based on the same cohesive zone concept. They are summarized in Figure 2-6:

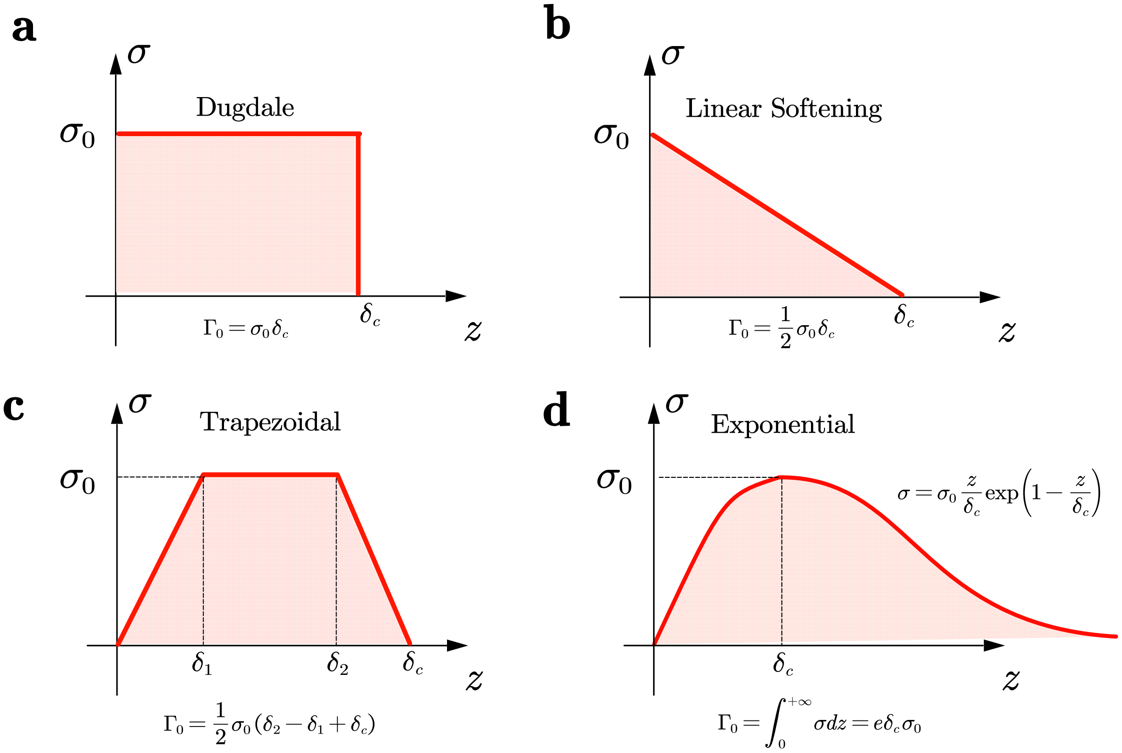

Figure 2-6: Different traction-separation laws based on cohesive zone concept. (a) Dugdale's constant stress. (b) Linear softening law. (c) Trapezoidal law and (d) Exponential law.

2.6.1 Implementation in Abaqus FEA

The built-in surface-based cohesive models in Abauqs FEA shares a similar principle with cohesive zone theories introduced earlier in this section. It's applicable in situations when the size of cohesive contact zone is negligible compared to the overall length scale of the body under consideration. When the state of deformation of the cohesive layer with finite thickness is concerned, another cohesive elements method is used to model the layer material as a continuum. Other than that, the constitutive response of interfaces in contact are well described by the traction-separation relations.

The surface-based modeling of cohesive interaction assumes a linear elastic stiffness up to the point of damage initiation when a criterion is met. The cohesive stiffness is degraded beyond the initiation point as dictated by the damage evolution law to simulate the effects of surface damage.

To account for the anisotropic behavior, the normal surface traction vector **t** and its three components $\{t_n, t_s, t_t\}$ along normal and two orthogonal directions in the plane of contact are related to the separation vector $\delta = \{\delta_n, \delta_s, \delta_t\}$ in the following matrix form [1]:

$$\mathbf{t} = \begin{Bmatrix} t_n \\ t_s \\ t_t \end{Bmatrix} = \begin{bmatrix} K_{nn} & K_{ns} & K_{nt} \\ K_{ns} & K_{ss} & K_{st} \\ K_{nt} & K_{st} & K_{tt} \end{bmatrix} \begin{Bmatrix} \delta_n \\ \delta_s \\ \delta_t \end{Bmatrix} = \mathbf{K}\delta \tag{2.24}$$

The stiffness matrix **K** is written in a more general uncoupled form to allow different components to be specified independently. Following the initial increase of surface traction, the onset of damage is governed by the initiation criterion which takes one of the four following representations [1]:

$$\max\left\{\frac{\langle t_n\rangle}{t_n^o}, \frac{t_s}{t_s^o}, \frac{t_t}{t_t^o}\right\} = 1 \tag{2.25}$$

$$\max\left\{\frac{\langle \delta_n\rangle}{\delta_n^o}, \frac{\delta_s}{\delta_s^o}, \frac{\delta_t}{\delta_t^o}\right\} = 1 \tag{2.26}$$

$$\left\{\frac{\langle t_n\rangle}{t_n^o}\right\}^2 + \left\{\frac{t_s}{t_s^o}\right\}^2 + \left\{\frac{t_t}{t_t^o}\right\}^2 = 1 \tag{2.27}$$

$$\left\{\frac{\langle \delta_n\rangle}{\delta_n^o}\right\}^2 + \left\{\frac{\delta_s}{\delta_s^o}\right\}^2 + \left\{\frac{\delta_t}{\delta_t^o}\right\}^2 = 1 \tag{2.28}$$

$$\tag{2.29}$$

where the material-dependent quantities $\{t_n^o, t_s^o, t_t^o\}$ and $\{\delta_n^o, \delta_s^o, \delta_t^o\}$ denote the threshold values of stresses and separations with their respective subscripts indicating the corresponding directions of action. The angle brackets signify that only tensile components could trigger the damage initiation. Subsequent degradation of the traction with further progressing separation is specified by the damage evolution law [1]:

$$t_n = \begin{cases} (1-D)\bar{t}_n, & \bar{t}_n \geq 0 \\ \bar{t}_n, & \text{otherwise} \end{cases} \tag{2.30}$$

$$t_s = (1-D)\bar{t}_s \tag{2.31}$$

$$t_t = (1-D)\bar{t}_t \tag{2.32}$$

in which $\{\bar{t}_n, \bar{t}_s, \bar{t}_t\}$ are stresses as predicated from the linear traction-separation law assuming no damage has been caused. The damage variable D can be expressed in the following two ways, corresponding to linear and exponential damage evolution, respectively [1]:

$$D_{\text{linear}} = \frac{\delta_m^f \left(\delta_m^{\max} - \delta_m^o\right)}{\delta_m^{\max}\left(\delta_m^f - \delta_m^o\right)} \tag{2.33}$$

$$D_{\text{exponential}} = 1 - \left\{\frac{\delta_m^o}{\delta_m^{\max}}\right\}\left\{1 - \frac{1 - \exp\left(-\alpha\left(\frac{\delta_m^{\max} - \delta_m^o}{\delta_m^f - \delta_m^o}\right)\right)}{1 - \exp(-\alpha)}\right\} \tag{2.34}$$

where $\delta_m = \sqrt{\langle\delta_n\rangle^2 + \delta_s^2 + \delta_t^2}$, and the superscripts o, f, max indicate the effective separation at initiation point, complete failure, and its maximum value reached in the loading history, correspondingly. Figure2-7 provides an illustration of the traction increase, damage initiation and evolution processes.

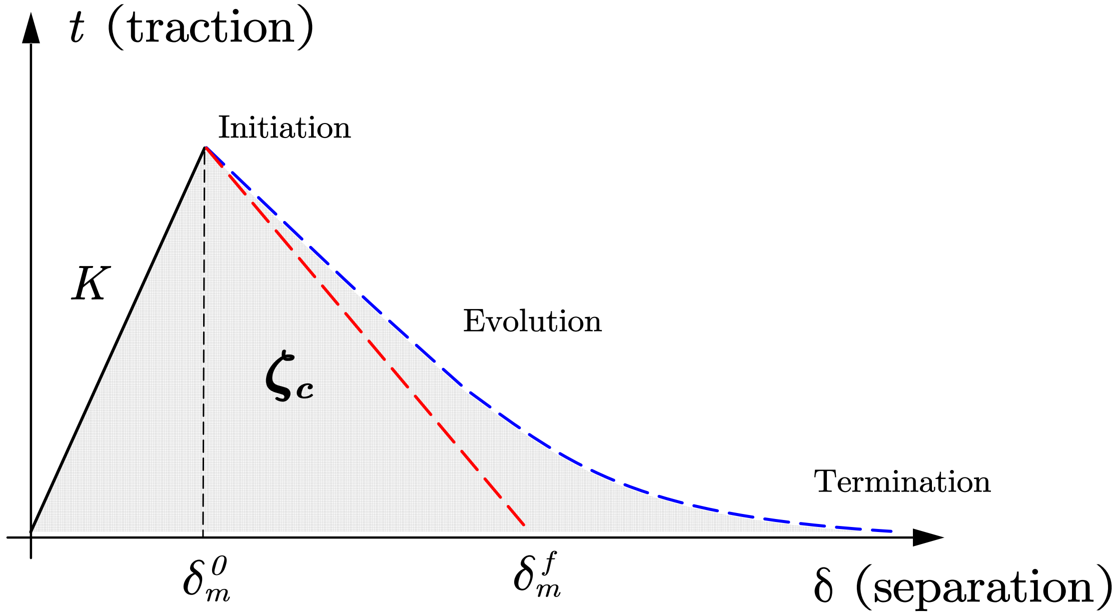
t (traction)
Initiation
K
Evolution
ζ_c
Termination
δ_m^0
δ_m^f
δ (separation)

Figure 2-7: Schematic representation of the surface-based cohesive contact model implemented in SIMULIA Abaqus. ζ_c indicates the dissipated energy due to surface failure and numerically equals the area under the curve. Beyond the damage initiation point, red dashed line represents the linear damage evolution while blue dashed line corresponds to the exponential evolution law.

Chapter 3

Finite Element Analysis of Interfacial Damage during Separation Process in Continuous 3D Printing

In the first chapter, the current state-of-the-art of the projection-based 3D printing technology has been reviewed. In particular, stereolithography generally replies on the absorption of light energy to activate the chain polymerization. Digital masks dictate the boundary of the light projection, while the actual termination of chain reaction is mediated by environmental and add-in inhibitors, commonly by reacting with oxygen to slow down the rate of propagation. Consequently the newly-formed interface exerts an attractive force between the bulk photopolymer and the oxygen-permeable substrate like PDMS, which obstructs the separation of the as-cured part from the substrate and the flow-in of fresh resin. To provide a more quantitative description of the process, and in view of all the adhesive contact mechanics models outlined in Chapter 2, I seek to implement the surface-based cohesive model into a numerical approach and deepen the understanding of interfacial contact in this chapter, particularly in the context of continuous microstereolithography. The first section will be dedicated to introduction of a infusion-based surface treating technique that effectively modifies interfacial adhesion, as the backbone of a published study which this thesis work is a part of [44], which also serves as the motivation of constructing the numerical model of this work to describe the separation behavior. The second section will feature the details of numerical implementation, followed by a simulated lifting test of a polymer disk being separated from different surfaces and benchmarked against experimental measurement on a force testing machine in the third section. After a clear understanding of a single pull-off event has been established, I will advance into the last section of this chapter where the lubricant-infused elastomer substrate is tested out in continuous 3D printing and its performances are evaluated. Repeated peeling off and associated degradation of the surface may provide additional insights into the kinetics of such fracturing process, and open up opportunities for future research along this line on the dynamics of such sticking and peeling off phenomena in a more general background.

3.1 Motivation for Adhesion Reduction Modeling and Sample Preparation in Continuous Stereolithography

In a typical configuration of bottom-up stereolithography with Digital Light Processing (DLP), projection of UV light comes from the bottom and curing happens at the bottom of the resin bath and liquid-solid interface. A critical challenge of the continuous 3D printing technology is that the overall performance is greatly limited by the strong bonding between polymer and substrate. This fact is illustrated in the following figure [44]:

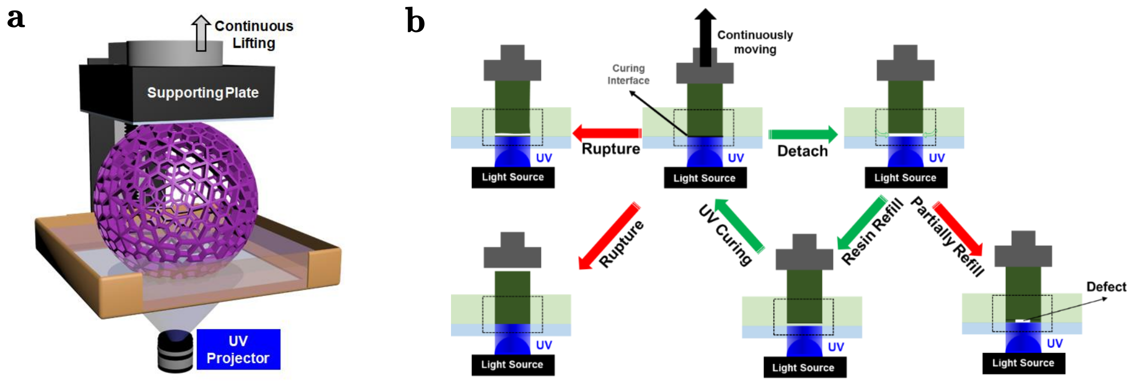
a
Continuous Lifting
Supporting Plate
UV Projector
b
Continuously moving
Curing Interface
Rupture
Detach
UV
Light Source
Rupture
UV Curing
Resin Refill
Partially Refill
Defect

Figure 3-1: (a) Schematic of a typical bottom-up continuous 3D printing configuration. (b) Illustration of abnormal situations that could happen at the interface during separation. The unfavorable solid-solid adhesion may obstruct the refill flow of liquid resin into the gap and result in structural defects in the newly formed layer. Alternatively, when the adhesion at curing interface exceeds the bulk fracture strength of polymer or the bonding strength at the top, the part is mostly likely to rupture which invalidates the whole printing process.

The limitation is two-fold. First of all, the interfacial condition will affect the rate of refill with resin of the gap created by elevating the cured layer away from the curing interface (Figure 3-2 (a)-(b)). The printer's moving stage would have to accommodate that by lowering the pulling-up speed. Secondly, the higher lifting velocity is correlated with larger projection light intensity, which in turns increases the adhesive force at the curing interface. The *in situ* measurements of the relationship between aforementioned physical quantities are summarized in Figure 3-2 (c)-(d) [44]:

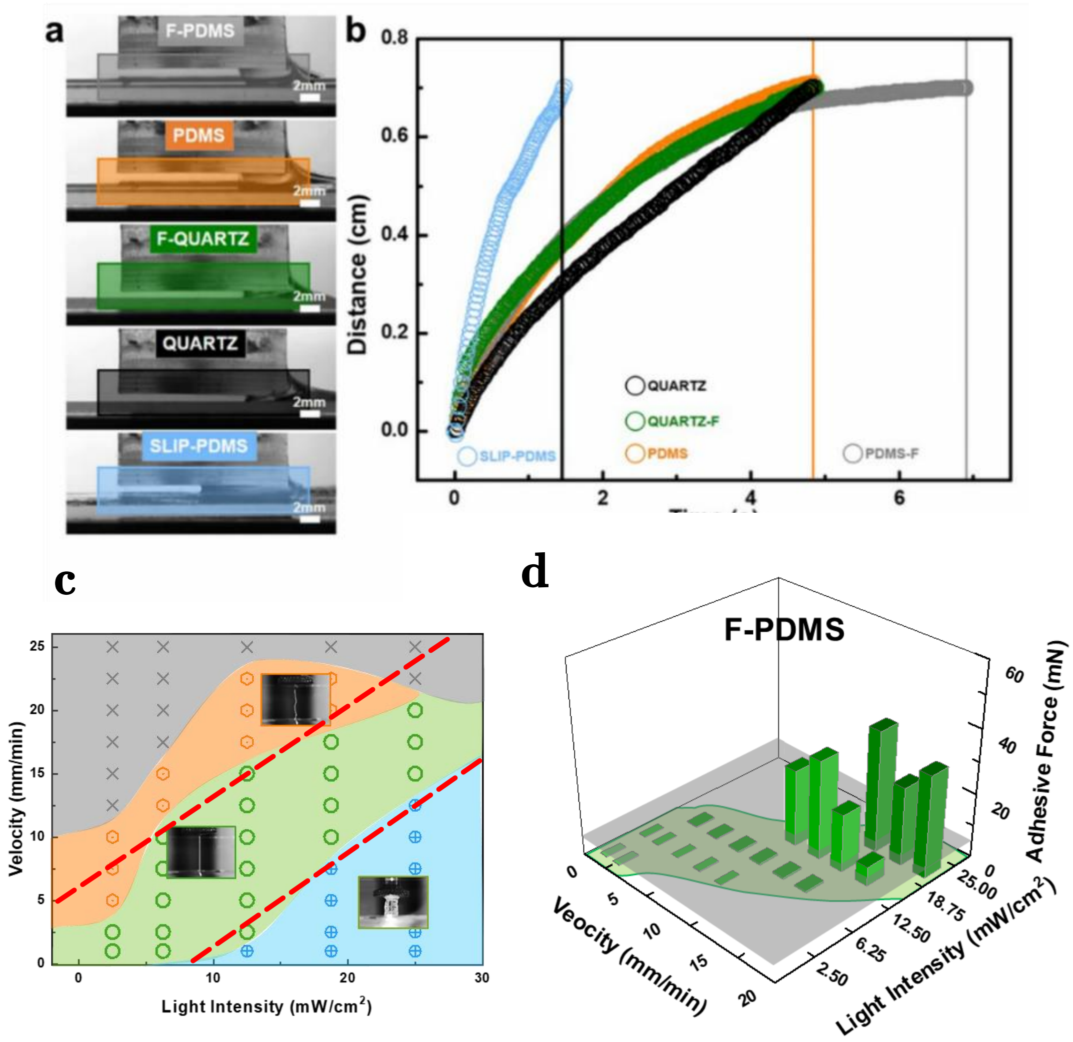

Figure 3-2: (a) Side view of liquid resin refilling the 1 mm gap between printed part and a variety of testing surfaces: fluorinated PDMS, regular PDMS, fluorinated quartz, quartz and lubricant-infused PDMS. (b) Real-time phase front tracking of liquid contact line as it moves across the gap. Total length of slit is 1.4 cm. (c) Correlation between moving speed of support plate and projection light intensity in continuous 3D printing. (d) 3D representation of the variation of adhesive force based on different printing velocities and light intensities.

To address these critical challenges, my collaborators Wu et al. got inspired by the slippery peristome surface of the pitcher plant and attempted to mimic the slipper water layer by creating an impregnable low adhesive lubricating interface that stably adheres to and preferentially wets the polymer network of the substrate than the impinging monomer resin immiscible with the lubrication liquid. This was achieved by immersing a cross-linked PDMS in perfluoro-carbon for 24 hours to ensure the functioning liquid penetrate into the polymer network and shield the PDMS solid from being contaminated or adhered to by the resin, effectively reducing adhesion along the surface normal. Additionally, the reduced friction at interface also allows resin liquid to roll on the surface freely and refill the gap efficiently. A close microscopic image of the surface morphology gave us a distribution of the hole size presented in the bar chart of Figure 3-3 (e). We shall defer the calculation of average capillary pressure that's stabilizing the liquid in the microcavities when we have quantitative data from numerical calculation of the pressure distribution at the top interface.

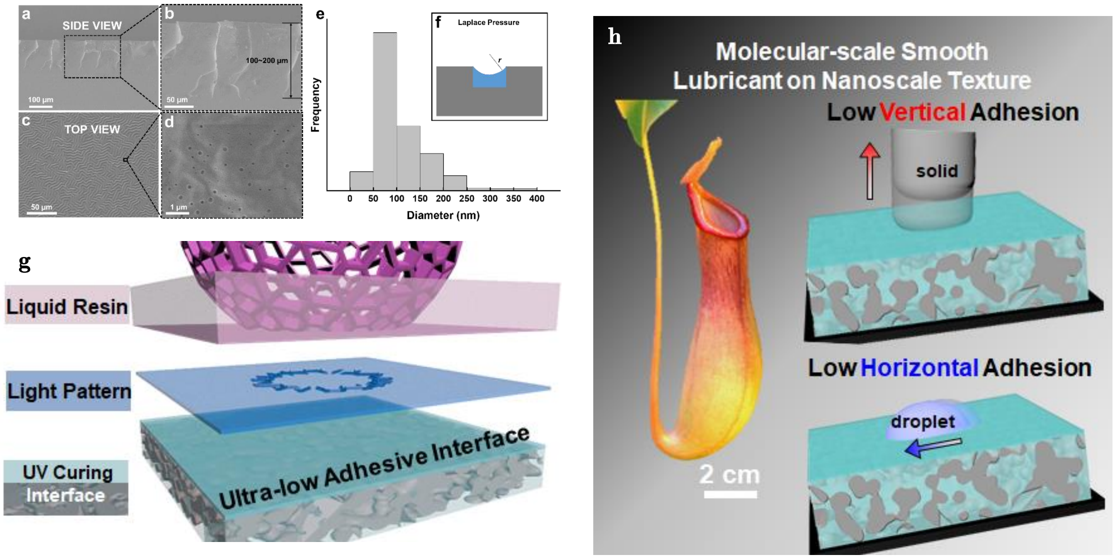
a
SIDE VIEW
100 µm
b
100~200 µm
50 µm
c
TOP VIEW
50 µm
d
1 µm
e
Frequency
0
50
100
150
200
250
300
350
400
Diameter (nm)
f
Laplace Pressure
r
g
Liquid Resin
Light Pattern
UV Curing Interface
Ultra-low Adhesive Interface
h
Molecular-scale Smooth Lubricant on Nanoscale Texture
Low Vertical Adhesion
solid
Low Horizontal Adhesion
droplet
2 cm

Figure 3-3: (a-b) Side view of the lubricant-infused PDMS and its enlarged local magnification. (c-d) Top view of the surface of lubricant-infused PDMS after treatment. (e) distribution of diameters of micro-holes. (f) Schematic of the Laplace pressure due to capillary effect that's holding back the liquid in the chamber. (g) A breakdown of the structural composition of the interfacial condition during 3D printing, and the illustration (h) showing the benefits of adhesion reduction along both normal and tangential directions.

Up to this point, we have established a relatively clear understanding from the microscopic view of the interface after lubrication treatment. In the next section, we will demonstrate how numerical modeling work can provide quantitative mechanical insights into this surface modification technique.

3.2 Rational Selection of Contact Mechanics Models

In Section 2.5 I reviewed the introduction of dimensionless Tabor for characterization of the relative importance of adhesion to elastic deformation. Along with many variants of it, Tabor number unifies and directs the transition between different contact models. A question remains is that in real practice how the work outlined in previous chapter helps us make rational decision on the appropriate model to use.

We shall revisit the adhesion map of adhesive contact models. Here I will reproduce the work done by Johnson and Greenwood [24], with some minor corrections of formulas.

First, in view of Figure 2-5 (a), the total adhesive and compressive force should be written as:

$$\begin{cases} P_{\mathrm{H}} = 4E^{*}a^{3}/3R \\ P_{\mathrm{D}} = -2\sigma_{0}\left[c^{2}\cos^{-1}\left(a/c\right) + a\sqrt{c^{2}-a^{2}}\right] \end{cases} \tag{3.1}$$

And the compression due to elastic deformation (as in Hertz contact) and due to adhesion, respectively,

$$\begin{cases} \delta_{\mathrm{H}} = a^{2}/R \\ \delta_{\mathrm{D}} = -\left(2\sigma_{0}/E^{*}\right)\sqrt{c^{2}-a^{2}} \end{cases} \tag{3.2}$$

After the non-dimensionalization transformation,

$$\bar{a} \equiv a\left(\frac{4E^{*}}{3\pi\mathit{\Delta}\gamma R^{2}}\right)^{1/3}; \bar{c} \equiv c\left(\frac{4E^{*}}{3\pi\mathit{\Delta}\gamma R^{2}}\right)^{1/3}; \bar{P} \equiv \frac{P}{\pi\mathit{\Delta}\gamma R} \tag{3.3}$$

The above expressions for forces become:

$$\begin{cases} \bar{P}_{\mathrm{H}} = \bar{a}^3 \\ \bar{P}_{\mathrm{D}} = -\lambda \bar{a}^2 \left[\sqrt{m^2 - 1} + m^2 \sec^{-1} m \right] \end{cases} \tag{3.4}$$

The equation (2.23) then can be expressed as,

$$\frac{\lambda \bar{a}^2}{2} \left[\left(m^2 - 2 \right) \sec^{-1} m + \sqrt{m^2 - 1} \right] + \frac{4 \lambda^2 \bar{a}}{3} \left[\sqrt{m^2 - 1} \sec^{-1} m - m + 1 \right] = 1 \tag{3.5}$$

along with the definition of transition parameter

$$\lambda \equiv \sigma_0 \left(\frac{9R}{2\pi \mathit{\Delta}\gamma \; E^{*2}} \right)^{1/3} \tag{3.6}$$

then for every data point with given λ, an additional equation is needed to solve for the set of equations (3.2), (3.4) and (3.5). The following chart summarizes the criteria and equations to solve for boundary lines between different models. After the boundary lines have been specified, the corresponding interfacial material properties can be added onto the plot by estimating their values from the pulling-off tests in Figure 3-7 (b). The vertical axis is the normalized net contact force acting on the body. Since the adhesive force is mainly concerned, all data points scatter on the lower half of the plot. The horizontal axis, elasticity parameter λ, characterizes the ratio between elastic deformation and adhesion. Quartz materials in the control group are much stiffer than the elastomers, thus locating along the left boundary

	Criterion	Equation
Hertz	$\lvert \bar{P}_a / \bar{P} \rvert < \xi$	$\bar{a} = \frac{(1+\xi)\lambda}{\xi} \left[m^2 \sec^{-1}(m) + \sqrt{m^2 - 1} \right]$
Bradley	$\lvert \delta_1 / h_0 \rvert < \zeta$	$\bar{a} = \sqrt{\frac{2\zeta}{\pi\lambda}}$
DMT	$\lvert \delta_a / h_0 \rvert < \eta$	$\frac{2\pi\lambda^2}{3\eta} \bar{a} \sqrt{m^2 - 1} = 1$
JKR	$\lvert \delta_a / h_0 \rvert > \chi$	$\frac{2\pi\lambda^2}{3\chi} \bar{a} \sqrt{m^2 - 1} = 1$

Table 3.1: Listing of all the criteria for determination of boundaries between different adhesive models. Additional equation is required to solve for the plot axis parameter. Separation criteria from [24].

of the section. Elastomers are much more compliant, and each surface treatment will give different adhesive energies, as dictated by their corresponding positions on the plot. The adhesion map not only helps elucidating the differences and guides the transition between various models, but also provides rationale for selecting the appropriate contact model based on material properties, as the Cohesive Zone theory has been chosen for this thesis work. The wide range of material properties tested in the work has made the Cohesive Zone Model best candidate for simulating the mechanical behaviors, and the details of numerical implementation will be laid out in the rest part of this chapter.

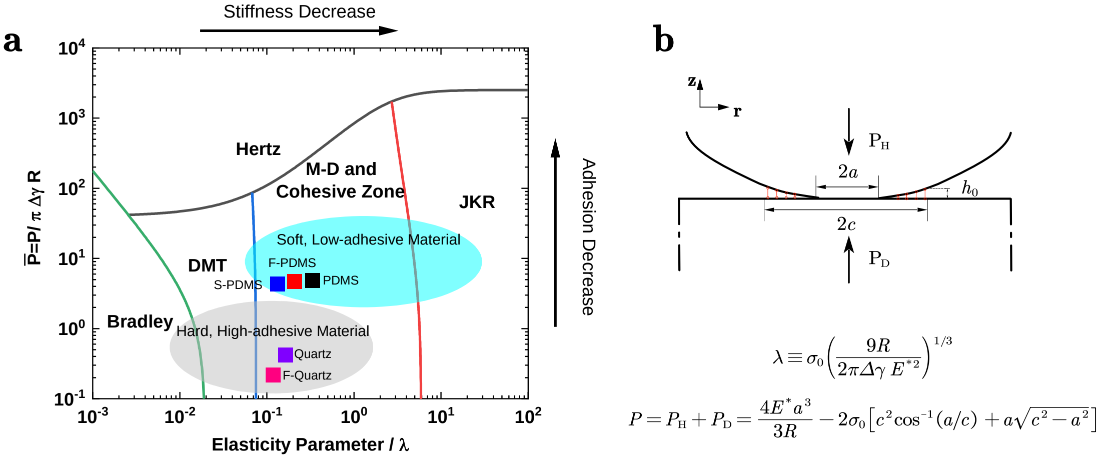

Figure 3-4: (a) Map of various adhesive contact models based on net contact force and elasticity parameter. Material properties are plotted on the adhesion map based on estimation from experimental data. (b) Schematic of the contact geometry with parameters used in the definitions of two coordinates of the map.

3.3 Modeling of adhesion with Surface-based Cohesive Contact implementation in Abaqus

The numerical analysis of the post-curing separation process allows us to map the physical quantities such as deformation, stress and surface properties from a continuum mechanics point of view to the macroscopic characterizations of the problem that are experimentally measurable, including pull-off force and displacement of the whole body. This will not only help us establish a gauging system to accurately evaluate different interfaces, but also grant physical insights into the contact problems and interfacial properties that are otherwise very difficult to consistently assess with experimental methods. Moreover, it also possesses the predicative capability to analyze more complicated problems when anisotropic surface movement and dynamic instability are involved. The last part will be delineated in more detail in the final chapter. To start with, I present the configuration of the numerical assembly in Figure 3-5. A cylindrical object representing photopolymer is assumed to be initially in full contact with the substrate block. The polymer material is modeled to be linearly elastic with Young's modulus $E = 2.6\,\mathrm{GPa}$, Poisson's ratio $\nu = 0.43$ and density $\rho = 1190\,\mathrm{kg\,m^{-3}}$. On the other hand, Neo-Hookean hyperelastic model is more suitable for the large deformation of the substrate, as we prescribe the shear modulus to be $\mu = 1.2\,\mathrm{MPa}$ and bulk modulus $K = 60.6\,\mathrm{MPa}$ with the following expression for free energy:

$$W = C_{10}\left(\bar{I}_1 - 3\right) + \frac{1}{D_1}\left(J_{e\ell} - 1\right)^2 \tag{3.7}$$

where $C_{10} = \mu/2$, $D_1 = 2/K$, $\bar{I}_1$ is the first strain invariant and $J_{e\ell}$ is the elastic volume strain. These material properties are globally applied not affected by different surface modifications. Below are the material-dependent properties we calibrate and tailor to meet the requirements of different interfacial conditions. The surface contact between bottom of polymer and top surface of substrate (coinciding with curing interface) is being modeled with the surface-based cohesive contact theory introduced in the previous chapter. I reiterate the model here in Figure 3-5 (b), with a schematic representation of the deforming process in Figure 3-5 (c) and a molecular picture of the contact situation in Figure 3-5 (d).

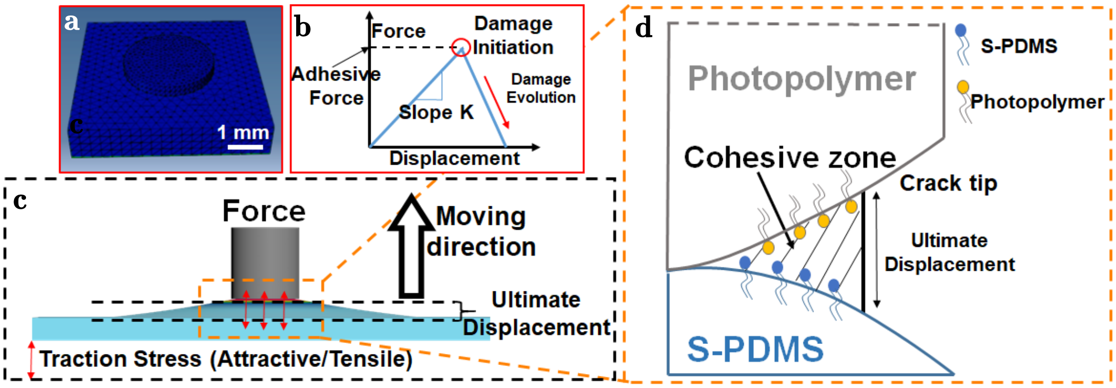

a
1 mm
b
Force
Damage Initiation
Adhesive Force
Slope K
Damage Evolution
Displacement
c
Force
Moving direction
Ultimate Displacement
Traction Stress (Attractive/Tensile)
d
Photopolymer
S-PDMS
Photopolymer
Cohesive zone
Crack tip
Ultimate Displacement
S-PDMS

Figure 3-5: (a) Configuration of the simulation. Photopolymer (cylindrical object) is in contact with the substrate (cuboid). (b)The constitutive relation in surface-based cohesive contact model (c) Schematic of the pulling up and deforming process during separation process in 3D printing. (d) Molecular picture of the cohesive interaction at the interface between photopolymer and substrate.

The interfacial contact conditions can be specified with the following set of parameters in Table 3.2.

	Quartz	F-Quartz	PDMS	F-PDMS	S-PDMS
K /N m^{-3}	7×10^{11}	2.9×10^{11}	3×10^{8}	2.3×10^{8}	3.45×10^{7}
t_n^o /kPa	1380	564	7.31	5.5	0.647
$t_s^o(t_t^o)$ /kPa	966	395	5.12	3.9	0.453
ζ_n^C /J m^{-2}	3.44	1.41	0.21	0.16	0.011
$\zeta_s^C(\zeta_t^C)$ /J m^{-2}	2.41	0.99	0.15	0.11	0.0077

Table 3.2: Listing of all the interfacial parameters for various surfaces simulated in this work. S-PDMS is the lubricant-infused PDMS and all the rest in the control groups are plain quartz surface (Quartz), fluorinated quartz surface (F-Quartz), untreated PDMS surface, and the fluorinated PDMS (F-PDMS) surface.

The boundary conditions are applied so the bottom of substrate is firmly fixed and the top of disk-shaped photopolymer is allowed to move along predefined trajectory, i.e. displacement controlled movement over a distance of 100 µm. The total force readout is obtained by summing up all the traction acting on individual element surface at the top. All of the parts in the assembly are meshed with 4-node tetrahedron elements and a static solver is selected to ensure the good convergence of the results.

3.4 Analysis of Numerical Simulation Results

The regular PDMS is tested out first. The von Mises stress distribution right before the total pull-off force reaches its peak is shown in Figure 3-6. The disk appears to be floating in the air due to the fact that this surface contact model we use has not accounted for the adhesive element that transmits the force between two adjacent interfaces in contact.The choice of model is well justified because this separation distance 40 µm is negligibly small compared with the overall size of both parts in contact, considering the typical sizes of a PDMS membrane and photopolymer in continuous 3D printing. The seemingly large separation in the snapshot is due to the fact that deformation is being displayed at 5X magnification for better visual effects, and that the disk's thickness has been capped at a minimal to reduce computational cost and truncate unnecessary details as we're not concerned about stress distribution in the bulk of polymer at this stage. From the stress distribution map, we see clearly the descending trends in the stress magnitude from regular to fluorinated and lubricant-infused PDMS. The stress is axisymmetric with respect to the center of contact, and its magnitude in general is declining from the edge of contact ring to the middle. This is arising from the fact that damage initially starts to from the fringe, resembling Mode I-opening mode in fracture mechanics, and propogates to the center. It's also evident from the deformed profile of substrate where the peak of protrusion at the middle is also closest to the disk bottom, and the distance is gradually ramping up as we move away from the center. According to traction-separation relation in Figure 2-7, the stress is monotonically increasing with larger separation distance before the damage starts to form. When the total reaction force on the photopolymer is plotted against the displacement, the accumulative effect of local adhesive contact interaction between two infinitesimal interfaces is manifesting itself in a very similar fashion as the traction-separation relation defined earlier in surface-based cohesive contact model. As shown in Figure 3-7 (c) [44], the force curve initially follows a linear increase, and then a near exponential decay after passing the peak. Note that unlike in the contact constitutive relation, in the total force-displacement curve dam-

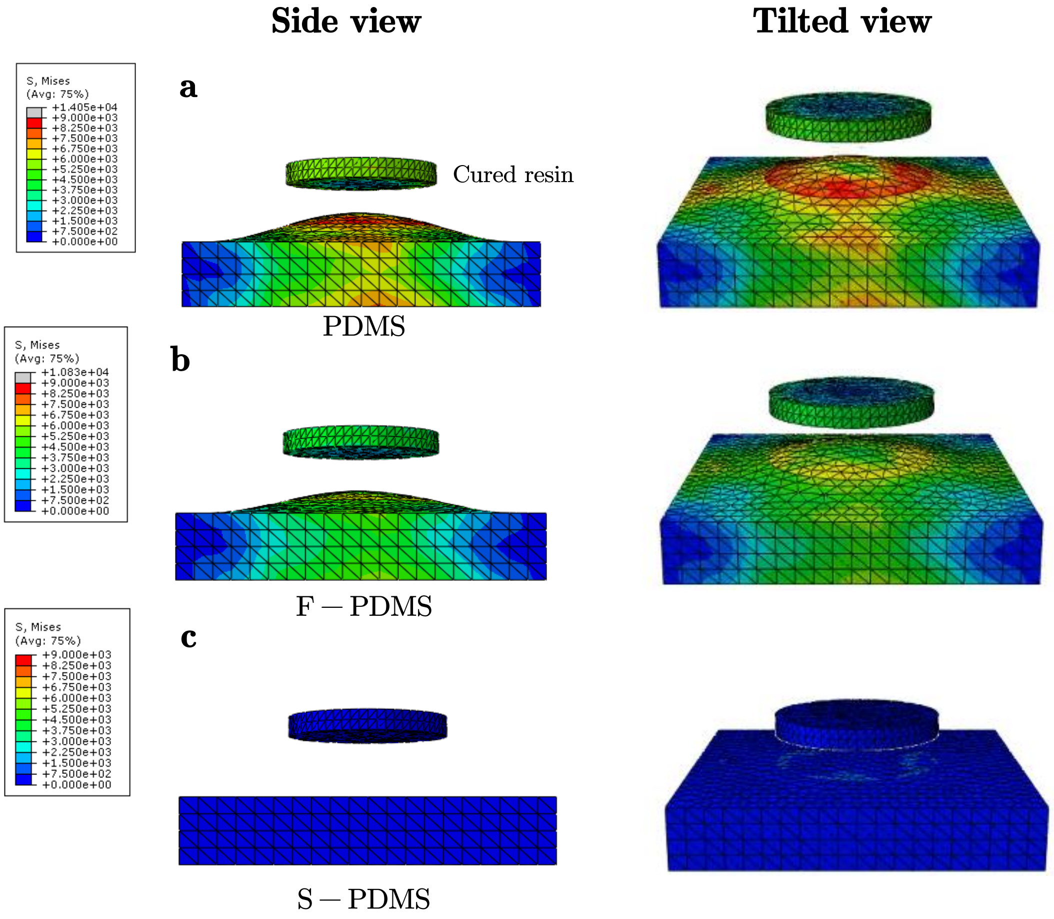
Side view
Tilted view
S, Mises
(Avg: 75%)
+1.405e+04
+9.000e+03
+8.250e+03
+7.500e+03
+6.750e+03
+6.000e+03
+5.250e+03
+4.500e+03
+3.750e+03
+3.000e+03
+2.250e+03
+1.500e+03
+7.500e+02
+0.000e+00
a
Cured resin
PDMS
S, Mises
(Avg: 75%)
+1.083e+04
+9.000e+03
+8.250e+03
+7.500e+03
+6.750e+03
+6.000e+03
+5.250e+03
+4.500e+03
+3.750e+03
+3.000e+03
+2.250e+03
+1.500e+03
+7.500e+02
+0.000e+00
b
F − PDMS
S, Mises
(Avg: 75%)
+9.000e+03
+8.250e+03
+7.500e+03
+6.750e+03
+6.000e+03
+5.250e+03
+4.500e+03
+3.750e+03
+3.000e+03
+2.250e+03
+1.500e+03
+7.500e+02
+0.000e+00
c
S − PDMS

Figure 3-6: Von Mises stress distribution for different substrate modifications: (a) Regular PDMS (b) fluorinated PDMS (F-PDMS) and (c) ultra-low adhesive energy interface (S-PDMS). Deformation field is magnified 5 times.

age had already been caused in part of the model before the top of curve was reached. A close comparison with experimental data displayed in Figure 3-7 (b) shows good consistency in trends. In the experimental measurement setup, the supporting plate is mounted on a load cell with the micro-displacement control stage, which measures the real-time vertical adhesion between the cured resin and the curing interface during the supporting plate lifting process. Elevated by the micro-displacement stage, the cured resin can be peeled off from the resin tank with a steady speed. A circular light pattern is projected onto the curing interface at constant light intensity from bottom.

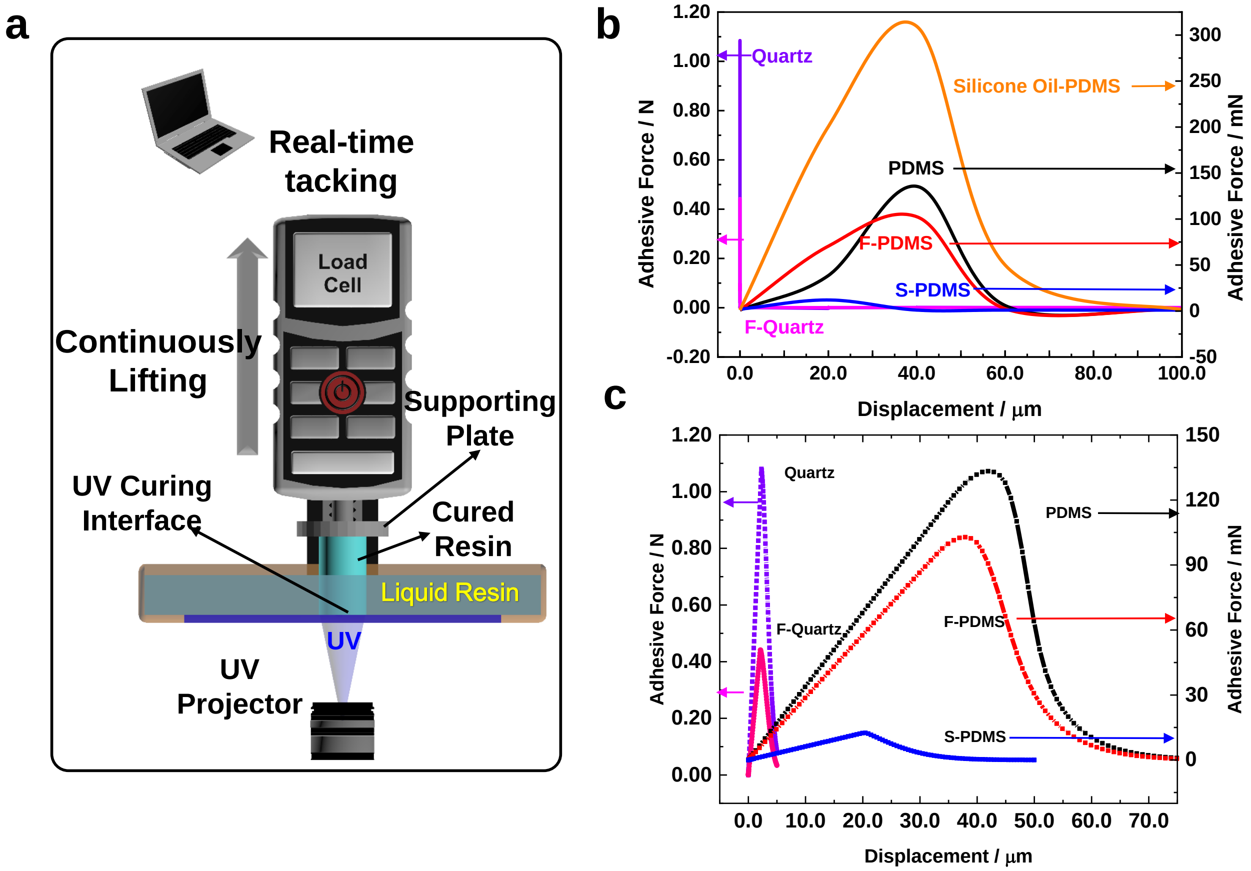

Figure 3-7: (a)Schematic of the experimental setup for force-displacement curve measurement. (b) Plotted experimental data of force and displacement in the peel-off test. Violet, magenta, black, red, orange and blue lines are force-displacement curves of Quartz, F-quartz, PDMS, F-PDMS, silicone oil swelled PDMS and the ultra-low adhesive S-PDMS interfaces, respectively. The data of quartz-based surfaces use the axis on the left and the data of the PDMS-based surfaces use the axis on the right and simulated results in (c).

3.5 Summary and prospects

In this chapter, I demonstrated the numerical implementation of surface-based cohesive contact model established in Chapter 2 using SIMULIA Abaqus. The simulation confirmed that after lubricant treatment, PDMS substrate exhibited a drastic decline of tendency to adhere to the cured polymer, which manifests in the flattened force-displacement curve. Not only did we see a significant decrease in the peak adhesive force, but also in the ultimate separation distance where the contact interaction between two interfaces terminates. The model introduced successfully establishes a connection between the macroscopic mechanical behavior of adhesive contact to a set of material-dependent parameters normally defined in a continuum contact mechanics framework. The model however, doesn't provide enough insights into the microscopic origins of those contact properties or propose a practical way of directly measuring them. Nevertheless, we may tentatively approach this by reexamining the SEM images of the surface of such lubricant-infused PDMS in Figure 3-3. The distribution of nano-cavities gave us an average size of around 100 nm, for instance. The capillary pressure resulted from surface tension can be estimated by:

$$\Delta P \equiv P_{\text{inside}} - P_{\text{outside}} = \gamma \left(\frac{1}{R_1} + \frac{1}{R_2} \right) \approx 2 \times \frac{15\,\mu\text{N}\,\text{m}^{-1}}{100\,\text{nm}} \approx 300\,\text{kPa} \tag{3.8}$$

which markedly exceeds the maximum traction stress of that surface listed in Table 3.2. This signifies that adhesive stress is highly unlikely to disrupt the equilibrium of perfluoro-carbon inside cavities maintained by capillary forces.

The modeling of the contact zone has also been simplified to neglect the influence of coexistence of two solid phases (PDMS substrate and impinging polymer) and two liquids (liquid resin and lubricant). During continuous 3D printing, surface energies and other interfacial conditions may non-trivially affect the transient break-up profile of viscoelastic fluid. As shown in Figure 3-8, various interfacial conditions show direct effects on the shape of resin undergoing transition from liquid to solid. The material properties of polymeric fluids are also related to the stretching of liquid filament, as exemplified by Figure 3-8 (i) and (j) showing the difference in persisting time and stretched shapes between Newtonian and viscoelastic liquids. How the collective effects of solid and liquid phases influence the printing speed and resolution of continuous 3D printing remains an intriguing yet open question.

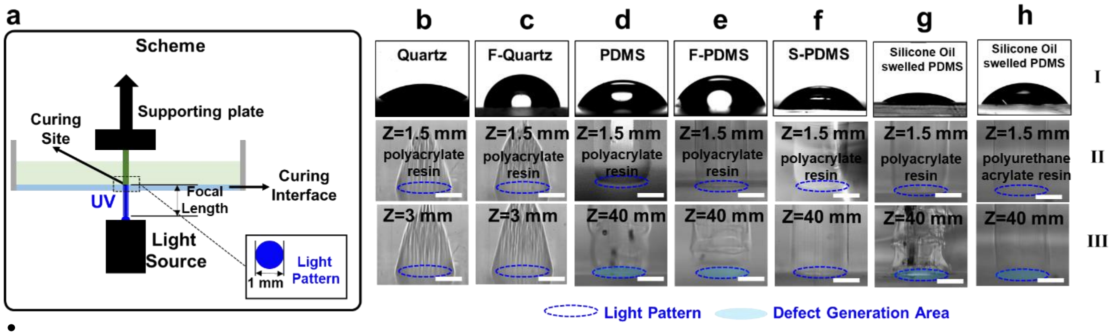
a
Scheme
Supporting plate
Curing Site
Curing Interface
UV
Focal Length
Light Source
1 mm
Light Pattern
b
c
d
e
f
g
h
Quartz
F-Quartz
PDMS
F-PDMS
S-PDMS
Silicone Oil swelled PDMS
Silicone Oil swelled PDMS
I
II
III
Z=1.5 mm
polyacrylate resin
polyurethane acrylate resin
Z=3 mm
Z=40 mm
Light Pattern
Defect Generation Area

i

(a) Styrene Oligomer

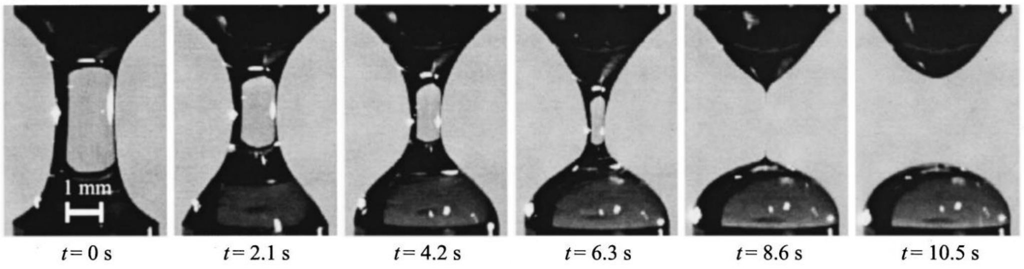
1 mm
$t = 0$ s
$t = 2.1$ s
$t = 4.2$ s
$t = 6.3$ s
$t = 8.6$ s
$t = 10.5$ s

j

(b) SM-1 Boger Fluid: 0.05 wt.% 2x10^6 g/mol polystyrene in styrene oligomer

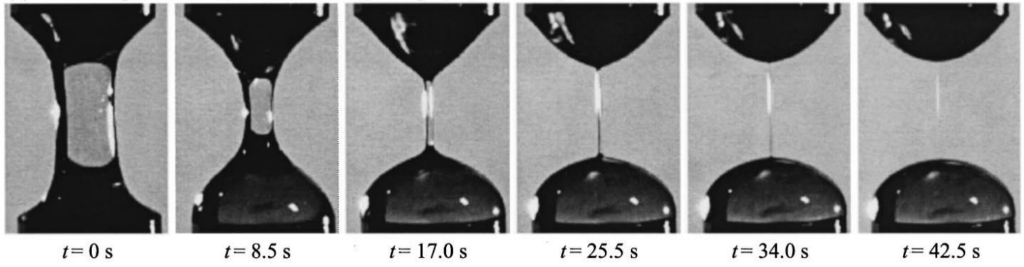
$t = 0$ s
$t = 8.5$ s
$t = 17.0$ s
$t = 25.5$ s
$t = 34.0$ s
$t = 42.5$ s

Figure 3-8: (a-h)Comparison of different interfaces during UV curing process. I shows different contact modes of impinging droplet on surfaces. II and III are optical images of resin morphology after plate has been lifted for a corresponding value of distance. [44] (i-j) Image sequences showing different transient liquid profiles of capillary thinning and breakup process for (i) Newtonian filament and (j) Boger fluid. [3]

Another important observation in experiment is the long-term degradation of surface quality due to continuous use. This becomes evident when we look at the load-displacement curves of different interfaces during continuous 3D printing over large distance (Figure 3-9). We even witnessed similar trends in long-term performance tests of S-PDMS surfaces. This leads to the question about the physical origins of these surface degradation that has not been captured by the simple Laplace pressure analysis above. It could include evaporation, wear-off of the elastomer substrate and contamination. I'll elaborate more in the final chapter as one of the future research possibility.

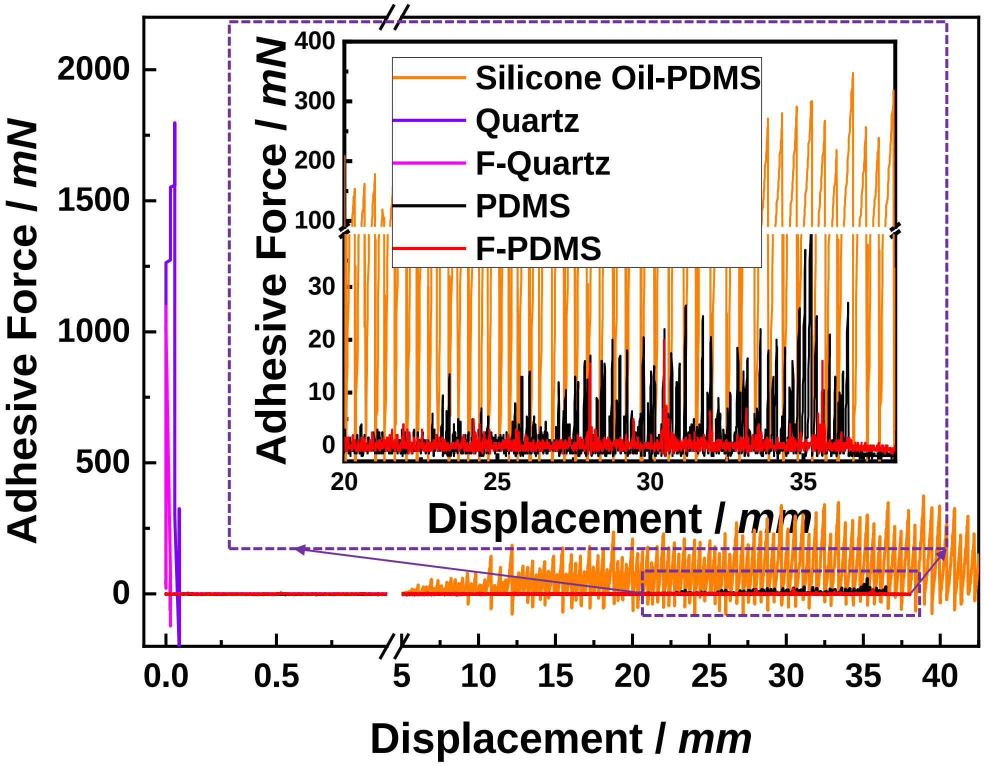

Figure 3-9: Long-term force-displacement curves for different interfaces during a complete continuous 3D printing process. Inset is the enlarged part of the force-displacement curve between 20 - 40 mm region for PDMS, F-PDMS and Silicone oil-PDMS surface. Violet, magenta, black, red and orange lines are force-displacement curves of Quartz, F-quartz, PDMS, F-PDMS and the silicone oil swelled PDMS interfaces, respectively.

Chapter 4

Conclusions and Future Work

In this thesis, I started from a background study of state-of-the-art of the adhesive force's impact on the performance metrics of 3D printing, and the lubricant-infused method as an emerging and promising solution to the problem. After a brief review of literature, the most important contact mechanics models were summarized in Chapter 2 to form a theoretical basis for the numerical implementation. From the basic non-adhesive Hertz Elastic Contact Model to the later Johnson-Kendall-Roberts (JKR) and Derjaguin-Muller-Toporov (DMT) Model and their respective extensions, they each have their own applicability in different situations, and Tabor number provides a unified governing criterion that guides the transition between different adhesion models. Figure 2-4 illustrates the range of applicability of these models on a two-parameter adhesion map, which allows the rational selection of appropriate theory for different application. Cohesive Zone Model along with its benefits and implementation in SIMULIA Abaqus is also elaborated.

After the theoretical foundation had been laid out, the surface-based cohesive contact model was carried out in analyzing a representative peel-out test of photopolymer from substrate during continuous 3D printing. The adhesive force at curing interface has been a critical challenge in achieving high speed and fine resolution of photo-crosslinking-based 3D printing technology, which significantly obstructs normal refill of liquid resin between layers and limits overall printing efficiency. By deploying a lubricant-infused method, it had been demonstrated to create a ultra-low adhesive energy interface which greatly reduces the adhesion in both normal and tangential direction. I consequently selected the proper material and contact mechanics theories to model the elastic deformation and cohesive contact of different curing interfaces encountered in 3D printing. The numerical implementation serves as a connection between the material-dependent contact properties from a continuum perspective and macroscopic mechanical behavior exhibiting as the force-displacement curve in a standard peel-off test. Not only did the simulated results show good consistency with experimental data, it also suggested useful physical insights into the stress distribution at the interface during separation, which also qualitatively explained why the lubricant-saturated nano-cavities remained relatively stable under cohesive interaction.

The limitation of the model was also discussed at the end of last chapter. Long-term degradation due to rubber wear-off poses another serious challenge of the application of this surface treatment. The dynamic process of crack initiation and propagation along the interface, with possible destructive impact on the bulk part of polymer as well, has largely remained a open problem to date. More generally, the soft cohesive contact problem under anisotropic interfacial moving conditions and repeated stick-separation-re-engagement has far-reaching impacts over various interdisciplinary fields across the boundary of material science, mechanics and acoustics. An exemplary case is given by stick-slip phenomenon in soft rubber contact. Due to the synergistic effects of adhesion and friction, the surface in contact buckles to form micro-ridges and cavities (as shown in Figure 4-1 (a)) which consequently propagate along the interface after nucleation and radiate acoustic energy into space because they usually contain small air pockets. Distinct with the peel-off process in 3D printing, the front and rear of contacting surfaces experience cyclic break-up and reformation of adhesive bonds, which is also indicated in the periodic oscillation of lateral force with time in Figure 4-1 (b). The propagating inhomogeneous modes of alternative stick and slip phases are historically termed as 'Schallamach waves' [37] and is the subject of multiple friction-adhesion induced noise control studies including squeaky rubber. The case demonstrated in this thesis comprises a small subset

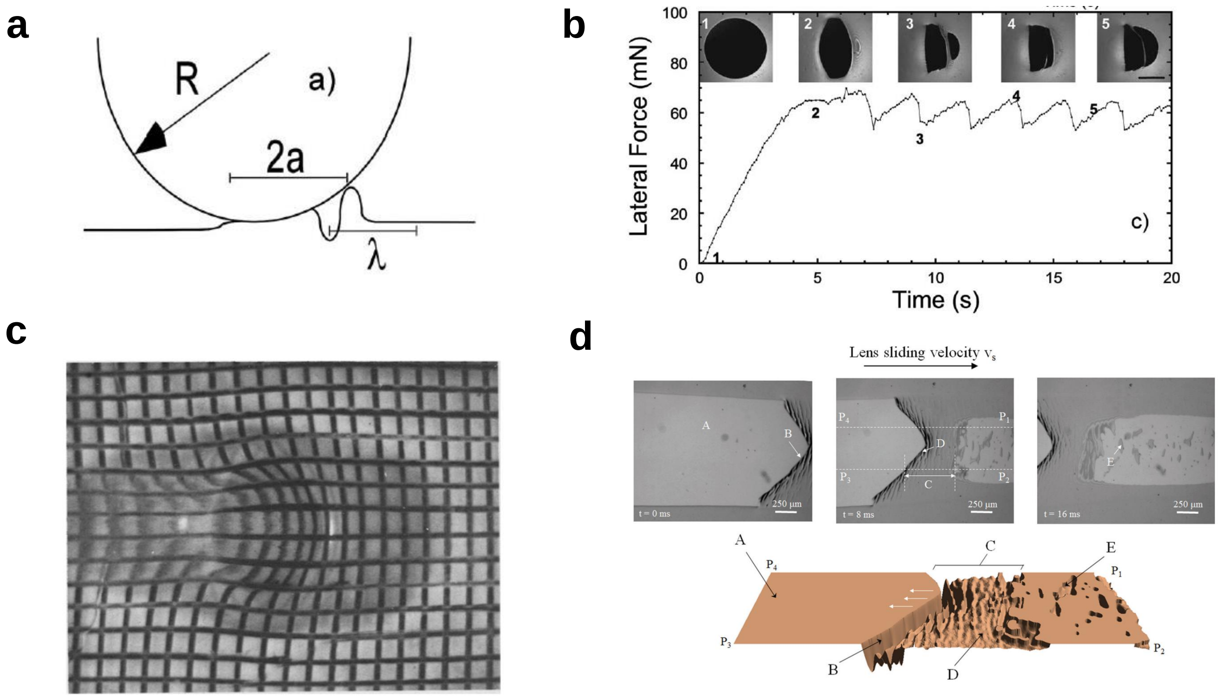

Figure 4-1: (a) Schematic of wrinkle of surface during adhesive contact. (b) Lateral force variable during rubber sliding and representative images of contact area. Scale bar 250 µm [35]. (c) Distortion of grid in a transparent rubbery material deformed by a rigid slider. [37]. (d) Wave front of Schallamach waves generated by a cylinder lens sliding on elastomer. Top row shows a solitary wave propagation and bottom panel is three-dimensional intensity plot of contact area morphology.A is undisturbed initial contact, and B is the wave front and C contains air cavities. E shows damaged surface after contact separation/wave passage and re-enter of adhesion. [41]

of the problems that are capable of being analyzed with the cohesive contact model proposed. Moreover, the modeling framework opens up possibilities for more comprehensive study of the dynamics of adhesive contacts involving the formation and propagation of instabilities.

Bibliography

[1] Version Abaqus. 6.14 documentation. *Dassault Systemes Simulia Corporation*, 651:6–2, 2014.

[2] Shahrouz Amini, Stefan Kolle, Luigi Petrone, Onyemaechi Ahanotu, Steffi Sunny, Clarinda N Sutanto, Shawn Hoon, Lucas Cohen, James C Weaver, Joanna Aizenberg, et al. Preventing mussel adhesion using lubricant-infused materials. *Science*, 357(6352):668–673, 2017.

[3] Shelley L Anna and Gareth H McKinley. Elasto-capillary thinning and breakup of model elastic liquids. *Journal of Rheology*, 45(1):115–138, 2001.

[4] Phil Attard and John L Parker. Deformation and adhesion of elastic bodies in contact. *Physical Review A*, 46(12):7959, 1992.

[5] Kellar Autumn, Yiching A Liang, S Tonia Hsieh, Wolfgang Zesch, Wai Pang Chan, Thomas W Kenny, Ronald Fearing, and Robert J Full. Adhesive force of a single gecko foot-hair. *Nature*, 405(6787):681, 2000.

[6] Kellar Autumn, Metin Sitti, Yiching A Liang, Anne M Peattie, Wendy R Hansen, Simon Sponberg, Thomas W Kenny, Ronald Fearing, Jacob N Israelachvili, and Robert J Full. Evidence for van der waals adhesion in gecko setae. *Proceedings of the National Academy of Sciences*, 99(19):12252–12256, 2002.

[7] Grigory Isaakovich Barenblatt. The mathematical theory of equilibrium cracks in brittle fracture. In *Advances in applied mechanics*, volume 7, pages 55–129. Elsevier, 1962.

[8] Etienne Barthel. Adhesive elastic contacts: Jkr and more. *Journal of Physics D: Applied Physics*, 41(16):163001, 2008.

[9] Bharat Bhushan and Eun Kyu Her. Fabrication of superhydrophobic surfaces with high and low adhesion inspired from rose petal. *Langmuir*, 26(11):8207–8217, 2010.

[10] Bharat Bhushan and Yong Chae Jung. Natural and biomimetic artificial surfaces for superhydrophobicity, self-cleaning, low adhesion, and drag reduction. *Progress in Materials Science*, 56(1):1–108, 2011.

[11] Bharat Bhushan, Yong Chae Jung, and Kerstin Koch. Micro-, nano-and hierarchical structures for superhydrophobicity, self-cleaning and low adhesion. *Philosophical Transactions of the Royal Society A: Mathematical, Physical and Engineering Sciences*, 367(1894):1631–1672, 2009.

[12] Rupert Stevenson Bradley. Lxxix. the cohesive force between solid surfaces and the surface energy of solids. *The London, Edinburgh, and Dublin Philosophical Magazine and Journal of Science*, 13(86):853–862, 1932.

[13] Jiaxi Cui, Daniel Daniel, Alison Grinthal, Kaixiang Lin, and Joanna Aizenberg. Dynamic polymer systems with self-regulated secretion for the control of surface properties and material healing. *Nature materials*, 14(8):790, 2015.

[14] J Davies, S Haq, T Hawke, and JP Sargent. A practical approach to the development of a synthetic gecko tape. *International Journal of Adhesion and Adhesives*, 29(4):380–390, 2009.

[15] Brian Dean and Bharat Bhushan. Shark-skin surfaces for fluid-drag reduction in turbulent flow: a review. *Philosophical Transactions of the Royal Society A: Mathematical, Physical and Engineering Sciences*, 368(1929):4775–4806, 2010.

[16] Huajian Gao, Xiang Wang, Haimin Yao, Stanislav Gorb, and Eduard Arzt. Mechanics of hierarchical adhesion structures of geckos. *Mechanics of Materials*, 37(2-3):275–285, 2005.

[17] Xuefeng Gao and Lei Jiang. Biophysics: water-repellent legs of water striders. *Nature*, 432(7013):36, 2004.

[18] Andre K Geim, SV Dubonos, IV Grigorieva, KS Novoselov, AA Zhukov, and S Yu Shapoval. Microfabricated adhesive mimicking gecko foot-hair. *Nature materials*, 2(7):461, 2003.

[19] JA Greenwood. Adhesion of elastic spheres. *Proceedings of the Royal Society of London. Series A: Mathematical, Physical and Engineering Sciences*, 453(1961):1277–1297, 1997.

[20] Caitlin Howell, Alison Grinthal, Steffi Sunny, Michael Aizenberg, and Joanna Aizenberg. Designing liquid-infused surfaces for medical applications: A review. *Advanced Materials*, 30(50):1802724, 2018.

[21] Biyu Jin, Mingzhu Liu, Qinghua Zhang, Xiaoli Zhan, and Fengqiu Chen. Silicone oil swelling slippery surfaces based on mussel-inspired magnetic nanoparticles with multiple self-healing mechanisms. *Langmuir*, 33(39):10340–10350, 2017.

[22] Kenneth Langstreth Johnson and Kenneth Langstreth Johnson. *Contact mechanics.* Cambridge university press, 1987.

[23] Kenneth Langstreth Johnson, Kevin Kendall, and AD Roberts. Surface energy and the contact of elastic solids. *Proceedings of the royal society of London. A. mathematical and physical sciences*, 324(1558):301–313, 1971.

[24] KL Johnson and JA Greenwood. An adhesion map for the contact of elastic spheres. *Journal of colloid and interface science*, 192(2):326–333, 1997.

[25] KL Johnson and JA Greenwood. An approximate jkr theory for elliptical contacts. *Journal of Physics D: Applied Physics*, 38(7):1042, 2005.

[26] Kerstin Koch, Bharat Bhushan, and Wilhelm Barthlott. Multifunctional surface structures of plants: an inspiration for biomimetics. *Progress in Materials science*, 54(2):137–178, 2009.

[27] Tanu Suryadi Kustandi, Victor Donald Samper, Dong Kee Yi, Wan Sing Ng, Pavel Neuzil, and Wanxin Sun. Self-assembled nanoparticles based fabrication of gecko foot-hair-inspired polymer nanofibers. *Advanced Functional Materials*, 17(13):2211–2218, 2007.

[28] Haeshin Lee, Bruce P Lee, and Phillip B Messersmith. A reversible wet/dry adhesive inspired by mussels and geckos. *Nature*, 448(7151):338, 2007.

[29] Khoon S Lim, Benjamin S Schon, Naveen V Mekhileri, Gabriella CJ Brown, Catherine M Chia, Sujay Prabakar, Gary J Hooper, and Tim BF Woodfield. New visible-light photoinitiating system for improved print fidelity in gelatin-based bioinks. *ACS Biomaterials Science & Engineering*, 2(10):1752–1762, 2016.

[30] Daniel Maugis. Adhesion of spheres: the jkr-dmt transition using a dugdale model. *Journal of colloid and interface science*, 150(1):243–269, 1992.

[31] Vahid Mortazavi and MM Khonsari. On the degradation of superhydrophobic surfaces: A review. *Wear*, 372:145–157, 2017.

[32] VM Muller, VS Yushchenko, and BV Derjaguin. On the influence of molecular forces on the deformation of an elastic sphere and its sticking to a rigid plane. *Journal of Colloid and Interface Science*, 77(1):91–101, 1980.

[33] Liangti Qu and Liming Dai. Gecko-foot-mimetic aligned single-walled carbon nanotube dry adhesives with unique electrical and thermal properties. *Advanced materials*, 19(22):3844–3849, 2007.

[34] Liangti Qu, Liming Dai, Morley Stone, Zhenhai Xia, and Zhong Lin Wang. Carbon nanotube arrays with strong shear binding-on and easy normal lifting-off. *Science*, 322(5899):238–242, 2008.

[35] Charles J Rand and Alfred J Crosby. Insight into the periodicity of schallamach waves in soft material friction. *Applied physics letters*, 89(26):261907, 2006.

[36] Wolf-Ernst Reif. *Squamation and ecology of sharks.* Senckenbergische Naturforschende Gesellschaft, 1985.

[37] A Schallamach. How does rubber slide? *Wear*, 17(4):301–312, 1971.

[38] Frank Schellenberger, Jing Xie, Noemí Encinas, Alexandre Hardy, Markus Klapper, Periklis Papadopoulos, Hans-Jürgen Butt, and Doris Vollmer. Direct observation of drops on slippery lubricant-infused surfaces. *Soft Matter*, 11(38):7617–7626, 2015.

[39] CT Sun and ZH Jin. Chapter 9-cohesive zone model, 2012.

[40] D Tabor. Surface forces and surface interactions. In *Plenary and Invited Lectures*, pages 3–14. Elsevier, 1977.

[41] Koushik Viswanathan, Anirban Mahato, and Srinivasan Chandrasekar. Nucleation and propagation of solitary schallamach waves. *Physical Review E*, 91(1):012408, 2015.

[42] Sanghyuk Wooh and Hans-Jürgen Butt. A photocatalytically active lubricant-impregnated surface. *Angewandte Chemie International Edition*, 56(18):4965–4969, 2017.

[43] Sanghyuk Wooh and Doris Vollmer. Silicone brushes: omniphobic surfaces with low sliding angles. *Angewandte Chemie International Edition*, 55(24):6822–6824, 2016.

[44] L Wu, Z Dong, H Du, C Li, NX Fang, Y Song, et al. Bioinspired ultra-low adhesive energy interface for continuous 3d printing: Reducing curing induced adhesion. *Research*, 2018:4795604, 2018.

[45] Shengsheng Yang, Ri Qiu, Hongqing Song, Peng Wang, Zhiqiang Shi, and Yanfang Wang. Slippery liquid-infused porous surface based on perfluorinated lubricant/iron tetradecanoate: preparation and corrosion protection application. *Applied Surface Science*, 328:491–500, 2015.

[46] Shuaishuai Yuan, Shifang Luan, Shunjie Yan, Hengchong Shi, and Jinghua Yin. Facile fabrication of lubricant-infused wrinkling surface for preventing thrombus formation and infection. *ACS applied materials & interfaces*, 7(34):19466–19473, 2015.

[47] Y-P Zhao, LS Wang, and TX Yu. Mechanics of adhesion in mems—a review. *Journal of Adhesion Science and Technology*, 17(4):519–546, 2003.